Diagnosing Forecast Errors in Tropical Cyclone Motion

THOMAS J. GALARNEAU JR. AND CHRISTOPHER A. DAVIS

National Center for Atmospheric Research, Boulder, Colorado*

(Manuscript received 12 March 2012, in final form 20 June 2012)

ABSTRACT

This paper reports on the development of a diagnostic approach that can be used to examine the sources of numerical model forecast error that contribute to degraded tropical cyclone (TC) motion forecasts. Tropical cyclone motion forecasts depend upon skillful prediction of the environment wind field, and by extension, the synoptic-scale weather systems nearby the TC. While previous research suggests that the deep-layer mean (DLM) steering flow typically approximates the actual TC motion, it is shown that the motion of even mature TCs can depart from the DLM steering flow. An optimal environmental steering flow is defined, which varies the vertical extent of the steering layer and the radius over which TC vorticity and divergence are removed.

Errors in predicted TC motion are quantified using a diagnostic equation that accounts for not only differences in the synoptic-scale flow, but also differences in the depth and radius used to define the steering flow. Differences in the latter two parameters are interpreted in terms of errors in predicted TC structure or errors in proximate mesoscale flow features. Results from an analysis of 24-h forecasts from the Advanced Hurricane Weather Research and Forecasting Model during the 2008–10 North Atlantic TC seasons show that forecast motion errors are dominated by errors in the environment wind field. Contributions from other terms are occasionally large and are interpreted from a vorticity perspective. The utility of this new diagnostic equation is that it can be used to assess TC motion forecasts from any numerical modeling system.

1. Introduction

North Atlantic tropical cyclone (TC) position (commonly referred to as ''track'') forecasts have shown great improvement over the last 40 years. Official National Hurricane Center (NHC) TC position forecasts have gained approximately 1 day in skill as 48-h position forecast errors during 2000–08 are comparable to 24-h position forecast errors during 1970–89, at about 100 km (Rappaport et al. 2009, their Fig. 3). Much of the increase in forecast skill can be attributed to improvements in model physics, increases in model resolution, and increases in the available aircraft and satellite observations (e.g., Aberson 2010). Additionally, improved data assimilation techniques have allowed for model initial conditions that more accurately represent the real atmosphere (e.g., Hamill et al. 2011). Despite consistent and substantial improvements in TC position forecasts, large errors still occur and can be particularly troublesome given the overall improvement that has occurred, and the societal expectations that accompany such improvement.

Numerous studies have examined factors—including environment wind errors and storm structure errors—that may lead to TC position forecast errors in numerical models. Carr and Elsberry (2000) found that TC position errors in the Navy Operational Global Atmospheric Prediction System model (NOGAPS) and the Geophysical Fluid Dynamics Laboratory hurricane model (GFDN) are commonly driven by errors in TC–midlatitude cyclone interaction. These types of errors can be related to errors in TC or midlatitude cyclone size and separation distance. Errors associated with TC-related anticyclone intensification aloft can also contribute to environment wind errors that may lead to poor TC position forecasts. Kehoe et al. (2007) found similar errors

* The National Center for Atmospheric Research is sponsored by the National Science Foundation.

Corresponding author address: Thomas J. Galarneau Jr., National Center for Atmospheric Research, P.O. Box 3000, Boulder, CO 80307.
E-mail: tomjr@ucar.edu

DOI: 10.1175/MWR-D-12-00071.1

for western North Pacific TCs in newer versions of the NOGAPS and GFDN.

While TC position forecast ''busts'' can be related to errors in the structure and intensity of the TC vortex (e.g., McTaggart-Cowan et al. 2006), errors in the environment wind appear to have the greatest effect on TC position errors. For example, position forecasts for TC Ike (2008) from three operational global models[1] initialized at 0000 UTC 9 September 2008 all steered TC Ike into south Texas, rather than recurved Ike over the Gulf of Mexico (Brennan and Majumdar 2011). This error in forecasted position was attributed to excessive zonal elongation of the subtropical anticyclone over the southern United States, which induced a more easterly steering flow over the Gulf of Mexico. This error in the structure of the subtropical ridge could be traced back to model environment initial condition errors (Komaromi et al. 2011).

Previous studies have offered numerous suggestions for the computation of steering flow for TCs. Mitchell (1924) posed that the movement of TCs in the North Atlantic basin was driven by the environment wind in the layer 3–5 km above mean sea level, and these winds were driven by the quasi-persistent subtropical anticyclone. George and Gray (1976) and others supported this notion by suggesting that flow near 700 mb, or in the 700–500-mb layer, best represents the environment wind that drives TC motion in the tropics. More recent studies have suggested that the deep-layer mean (DLM) wind is the best discriminator for TC motion for well-developed TCs (e.g., Sanders et al. 1980; Dong and Neumann 1986; Velden and Leslie 1991). In all, previous studies agree that TC motion is driven primarily by the environment flow (e.g., Chan and Gray 1982; Holland 1983, 1984; Chan et al. 2002 and references therein)—which involves removal of the wind field associated with the TC vortex (e.g., Neumann 1979; Fiorino and Elsberry 1989)—that is comprising flow contributions from nearby synoptic-scale weather systems and from asymmetric circulations (i.e., beta effect) induced by the TC itself (e.g., Holland 1983; Fiorino and Elsberry 1989; Carr and Elsberry 1990; Wu and Emanuel 1993). Tropical cyclone motion can also be influenced by features and processes not explicitly included in the environment flow, such as the interaction with landmasses (e.g., Holland 1983) and the underlying ocean (e.g., Bender et al. 1993; Chan et al. 2001), and effects from an asymmetric distribution of convection within the TC circulation typically driven by balanced motions associated with a vortex embedded in vertical shear (e.g., Wang and Holland 1996).

The aim of this study is to develop a new technique for diagnosing forecast errors in TC motion. To do this, we will present a new method for computing TC steering flow that allows the vertical depth of the steering layer and the radius of TC removal to vary in order to obtain the optimal match between the steering flow and actual TC motion. We can then use the optimal steering flow and actual TC motion to develop and use a diagnostic equation that will quantitatively determine the sources of error in the 24-h forecasts from the Advanced Hurricane Weather Research and Forecasting Model (AHW; Skamarock et al. 2008; Davis et al. 2008a) that contribute to large errors in TC motion. The motion error diagnostic will be examined from a statistical perspective for the 2008–10 North Atlantic TC seasons, and from a case study perspective for TCs Earl (2010) and Fiona (2010) (Fig. 1). We examine the motion vector errors at 24 h in the AHW forecast because at this time we are relatively certain that geographical differences in TC position have a minor contribution to environment wind forecast errors. Nonetheless, motion errors early in the forecast can lead to large position errors at longer lead times.

This paper is organized as follows. Section 2 describes the datasets used and the method for computing TC steering flow and motion error diagnostic. The TC steering flow and motion error diagnostic statistical results are presented in section 3. A brief synoptic overview of TCs Earl and Fiona is provided in section 4. Motion error diagnostic analysis of TCs Earl and Fiona are presented in sections 5 and 6, respectively. Section 7 provides the conclusions.

2. Data and methods

a. Analyses and forecasts

The analyses presented herein are generated from several datasets for both observed and AHW forecasts of TCs. The North Atlantic Hurricane Best Track Database (HURDAT; Jarvinen et al. 1984) was used to determine the observed positions of TCs. We computed the motion of TCs based on the HURDAT positions at 12 h before and after the observation time of interest. Diagnostic analyses, including the computation of steering flow, were derived using the National Centers for Environmental Prediction (NCEP) Climate Forecast System Reanalysis (CFSR; Saha et al. 2010) available 4 times daily at $0.5° \times 0.5°$ horizontal resolution and 50-mb (25-mb resolution below 750 mb)

[1] The National Centers for Environmental Prediction (NCEP) Global Forecast System (GFS), European Centre for Medium-Range Weather Forecasts (ECMWF), and Met Office (UKMO) operational models.

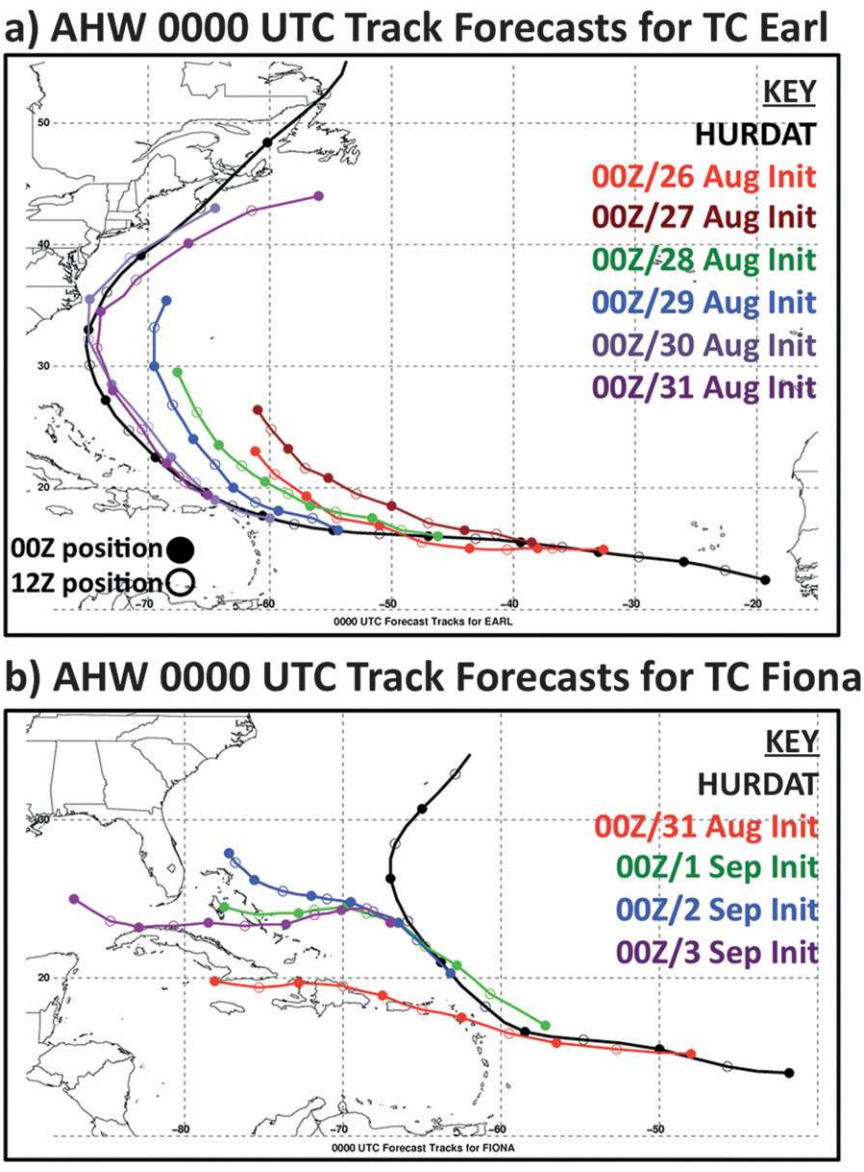

FIG. 1. HURDAT (black line) and AHW (colored lines) track forecasts initialized at 0000 UTC for (a) TC Earl and (b) TC Fiona. The TC Earl 0000 UTC forecasts are shown for 26–31 Aug 2010 and TC Fiona for 31 Aug–3 Sep 2010. The track forecasts are color coded by the key. The 0000 (1200) UTC positions are marked by filled (unfilled) circles.

vertical resolution. For the AHW forecasts, the TC positions were determined by locating and tracking the 850-mb geopotential height minimum. This tracking methodology is most successful for well-defined TCs, and can occasionally have difficulty correctly tracking systems that are weaker than tropical storm strength. To address this potential problem with TC positions identified by the tracker, each forecasted TC track in AHW was manually inspected and corrected (if necessary) by examining 6-hourly 850-mb geopotential height and relative vorticity maps. As with the observed TCs, the positions at 12 h before and after the time of interest were used to compute the motion of the forecasted TC.[2]

The numerical forecasts of TCs were generated using version 3.3 of the AHW with 36 vertical levels up to 20 mb (Skamarock et al. 2008). Details of the AHW are

[2] The positions at ±12-h were used to help reduce the impact of short-term (6 hourly) variations in track that can occur in AHW because of storm-scale convective processes on the computation of storm motion.

TABLE 1. AHW version 3.3 model specifics for 2011 real-time and 2008–10 retrospective TC forecasts. Multiple entries indicate model configurations for domains 1, 2, and 3. The model domains are depicted in Fig. 2. Detailed descriptions of model settings are available in Skamarock et al. (2008) and Davis et al. (2008a).

Model parameter	Configuration
Horizontal grid spacing (km)	36.0, 12.0, 4.0[a]
Vertical levels	36, 36, 36
Time step (s)	180, 60, 20
Initial condition	Ensemble Kalman filter (EnKF) 6-h cycles[b]
Boundary condition	0.5° GFS
Cumulus convection	Tiedtke,[c] Tiedtke,[c] explicit
Boundary layer	Yonsei University (YSU; Hong et al. 2006)
Mixed-layer depth and SST	Hybrid Coordinate Ocean Model (HYCOM) ocean analysis
Microphysics	WRF single-moment 6-class microphysics scheme (WSM6; Hong et al. 2004)
Land surface	Noah (Ek et al. 2003)
Turbulence	2D Smagorinsky
Shortwave radiation	Goddard (Chou and Suarez 1994)
Longwave radiation	Rapid Radiative Transfer Model (Mlawer et al. 1997)
Diffusion	Second-order diffusion
Scalar advection	Positive definite
Wind-dependent drag formulation	Donelan
Wind-dependent enthalpy surface fluxes	Garratt

[a] The 12- and 4-km domains are moving nests.
[b] 96-member WRF-ARW ensemble, 36-km horizontal resolution, 36 vertical levels up to 20 mb, WSM6 microphysics, YSU PBL, and Noah land surface model. Analyses are generated every 6-h by assimilating surface pressure, rawinsonde data, dropsonde data, aircraft data, Aircraft Communications Addressing and Reporting System (ACARS), cloud winds, and TC position and minimum sea level pressure (Torn and Davis 2012). [Available online at http://www.atmos.albany.edu/facstaff/torn/atlenkf/.]
[c] More information on the modified Tiedtke convective parameterization scheme can be found in Zhang et al. (2011).

described in Davis et al. (2008a). This implementation of the AHW is summarized in Table 1. All forecasts are run over the 36-km domain illustrated on Fig. 2. The two-way moving nests of 12 and 4 km are located within the 36-km domain, and the movement of these nests is determined by the TC's motion during the previous 6 h. The 2011 version of AHW was run retrospectively for the North Atlantic TC seasons of 2008–10, specifically for the TCs listed on Table 2, and the 0000 UTC initializations are the subject of the analysis herein. In this manuscript, retrospective 24-h AHW forecasts of TC Earl and Fiona initialized at 0000 UTC 26–31 August 2010 and 31 August–3 September 2010, respectively, are

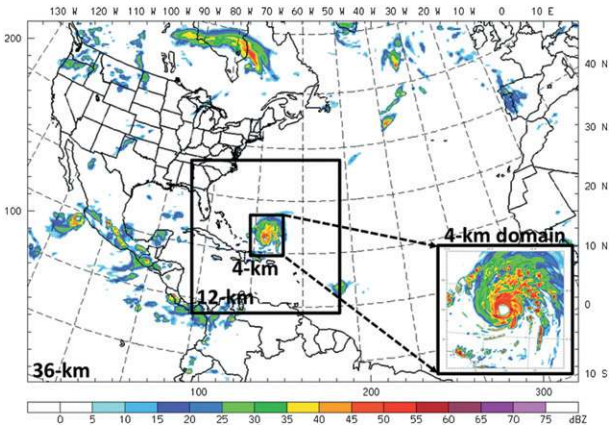

FIG. 2. Geographical location of the AHW model domains. The horizontal grid spacing on the outer domain is 36 km, and on the inner two domains are 12 and 4 km. The two inner domains are moving nests centered on the TC of interest. For illustrative purposes, the 72-h forecast initialized at 0000 UTC 29 Aug 2010 of composite reflectivity (shaded according to the color bar in dB*Z*) for TC Earl on the outer domain is shown. Reflectivity on the inner 4-km domain is also shown in the inset.

examined in more detail. Since we are only interested in the environment wind field and not necessarily the exact structure of the TC vortex (since the TC vortex is removed as described below), analyses are performed exclusively using the 36-km domain in AHW.

b. *Steering flow definition*

The environment wind is the residual wind that results from the removal of local winds associated with the TC vortex. Hence, the environment wind is driven by synoptic- and mesoscale features in the vicinity of the TC and by subsynoptic-scale asymmetric circulations

TABLE 2. List of North Atlantic TCs during the retrospective period (2008–10) that were rerun using the 2011 version of AHW.

2008	2009	2010
Fay	Ana	Danielle
Gustav	Bill	Earl
Hanna	Claudette	Fiona
Ike	Danny	Gaston
	Erika	Hermine
	Fred	Igor
	Ida	Julia
		Karl
		Lisa
		Matthew
		Nicole
		Otto
		Paula
		Richard
		Shary
		Tomas

(e.g., beta gyres) that are generated by the circulation of the TC itself (e.g., Fiorino and Elsberry 1989). The steering flow is the spatially averaged environment wind that matches the TC motion, and so is a function of the environment wind. To compute the steering flow for a TC, we must first compute an environment wind in layers that begin at 850 mb and increase upward to 200 mb at increments of 50 mb. To determine the environment wind with the circulation of the TC vortex removed, we follow the methodology in Davis et al. (2008b). For each disturbance, the vortex is removed at all vertical levels between 850 and 200 mb within a given radius using the Poisson equation for streamfunction (1) and velocity potential (2) with homogeneous boundary conditions applied at the edge of the computational domain.[3] The boundary value problem on each pressure level can be stated as

$$\nabla^2\psi = \begin{pmatrix} \zeta & \text{for} & r \le r_0 \\ 0 & \text{for} & r > r_0 \end{pmatrix}, \tag{1}$$

$$\nabla^2\chi = \begin{pmatrix} \delta & \text{for} & r \le r_0 \\ 0 & \text{for} & r > r_0 \end{pmatrix}, \tag{2}$$

where ψ is the streamfunction, χ is the velocity potential, $\psi = \chi = 0$ on the lateral boundaries of the computational domain, ζ is the relative vorticity, δ is the divergence, and r_0 is the radius of TC removal. Given the solutions for streamfunction and velocity potential from (1) and (2), we can determine the nondivergent and irrotational wind vectors from

$$\mathbf{V}_\psi(x,y,p) = \mathbf{k} \times \nabla\psi \tag{3}$$

and

$$\mathbf{V}_\chi(x,y,p) = \nabla\chi. \tag{4}$$

By subtracting (3) and (4) from the total wind $\mathbf{V}$ as follows

$$\mathbf{v}_{\text{env}}(x,y,p) = \mathbf{V}(x,y,p) - \mathbf{V}_\psi(x,y,p) - \mathbf{V}_\chi(x,y,p), \tag{5}$$

we have now computed the environment wind in which the TC is embedded with the effect of the TC circulation removed for a given r_0.

After removing the TC vortex as described above, we compute the area average of $\mathbf{v}_{\text{env}}$ for the observed[4] ($\mathbf{v}_{\text{obs}}$) and model ($\mathbf{v}_{\text{ahw}}$) TC within the chosen TC removal radius r_0:

$$\mathbf{v}_o(p) = \frac{1}{\pi r_o} \int_0^{2\pi} \int_0^{r_o} \mathbf{v}_{\text{obs}}(x,y,p) r\, dr, \tag{6}$$

$$\mathbf{v}_m(p) = \frac{1}{\pi r_m^2} \int_0^{2\pi} \int_0^{r_m} \mathbf{v}_{\text{ahw}}(x,y,p) r\, dr, \tag{7a}$$

$$\hat{\mathbf{v}}_m(p) = \frac{1}{\pi r_o^2} \int_0^{2\pi} \int_0^{r_o} \mathbf{v}_{\text{ahw}}(x,y,p) r\, dr, \tag{7b}$$

where $\mathbf{v}_o$ and $\mathbf{v}_m$ are the area-average environment wind and r_o and r_m are the TC removal radii for the observed and model TC, respectively. Additionally, $\hat{\mathbf{v}}_m$ is the area-average environment wind for the model TC using the best match radius for the observed TC. The environment wind is averaged horizontally over the same radius within which vorticity and divergence are set to zero. While not essential, it prevents introducing another length scale to the calculation. Under the assumption that TC motion corresponds to some spatial average of the environmental wind, we calculate the steering flow that best matches the actual motion of the TC by allowing the averaging scales to vary. To do this, we compute an area-average environment wind every 50 mb in the 850–200-mb layer as described above using eight different radii ranging from 1°–8° from the TC center whose location is assumed to not vary with pressure level. Then for each of the eight radii of TC removal, we compute the pressure-weighted vertical average of environment wind for layers of increasing depth ranging from the shallowest layer of 850–800 mb to the deepest layer of 850–200 mb. The combination of eight possible radii and 13 possible vertical averaging layers results in 104 possible steering layer wind values at a given time. For each candidate steering layer wind, the magnitude of the vector difference between the actual TC motion and the steering flow is computed. The radius and steering layer depth combination that produces the smallest vector residual magnitude is the steering layer definition chosen for the TC at a given time. For example, the observed steering flow residual matrix for TC Earl at 0000 UTC 28 August 2010 is shown

[3] The calculations shown herein were computed on a subregion of the CFSR and AHW grids covering 2°S–50°N and 105°–15°W [~(5778 km × 8858 km)] comprising 181 × 105 grid points with 0.5° gridpoint spacing. Note that using a grid smaller than the Rossby radius of deformation in the tropics [~(4000–6000 km on a side)] will introduce errors into the nondivergent and irrotational wind calculation.

[4] The steering flow for the observed TC is derived from the 0-h CFSR forecasts.

TABLE 3. Example of the observed steering flow residual matrix for TC Earl at 0000 UTC 28 Aug 2010. The steering flow residual is the magnitude (m s^{-1}) of the vector difference between the observed motion based on the HURDAT positions at ±12 h and the environment flow computed from the CFSR at all possible TC removal radii and vertical depths. The value in bold is the smallest vector residual, and hence defines the vertical depth (mb) and TC removal radius (°) chosen at that time. The bottom of the steering layer is fixed at 850 mb, therefore a 450-mb-deep steering layer is defined as the 850–400-mb layer.

	Depth (mb)												
Radius (°)	50	100	150	200	250	300	350	400	450	500	550	600	650
1	3.1	2.8	2.6	2.4	2.3	2.1	1.9	1.5	1.3	1.1	1.2	1.5	1.8
2	1.9	1.6	1.2	0.8	0.6	0.5	0.5	0.5	0.4	0.3	0.3	0.5	0.6
3	1.6	1.5	1.2	0.6	0.3	0.4	0.5	0.6	0.6	0.5	0.3	0.24	0.23
4	2.2	2.1	1.9	1.5	1.1	0.8	0.6	0.4	**0.19**	0.20	0.4	0.5	0.5
5	3.1	2.9	2.5	2.1	1.8	1.4	1.2	1.1	1.0	1.1	1.2	1.2	1.1
6	3.6	3.4	2.9	2.5	2.1	1.8	1.7	1.7	1.7	1.7	1.7	1.7	1.6
7	4.4	4.2	3.8	3.4	3.0	2.7	2.6	2.6	2.6	2.6	2.6	2.5	2.4
8	5.2	5.1	4.9	4.4	4.0	3.8	3.6	3.6	3.6	3.5	3.6	3.5	3.5

in Table 3. The optimal steering flow—defined as the radius and vertical depth combination that best matches the actual TC motion—is the pressure-weighted vertically integrated environment wind in the 850–400-mb layer using a radius of 4°. The same methodology is used to determine the steering depth (p_m) and radius (r_m) for the model TC.

After determining the optimal steering vertical depth and radius, we can equate the actual storm motion in observations ($\mathbf{V}_o$) and the model ($\mathbf{V}_m$), computed using the TC positions at 12 h before and after the current time, with the pressure-weighted vertical integral of the environment wind (e.g., the steering flow) computed using the optimal radius:

$$\mathbf{V}_o = \frac{1}{p_b - p_{t,o}} \int_{p_{t,o}}^{P_b} \mathbf{v}_o(p)\, dp, \tag{8}$$

$$\mathbf{V}_m = \frac{1}{p_b - p_{t,m}} \int_{p_{t,m}}^{P_b} \mathbf{v}_m(p)\, dp, \tag{9}$$

where p_b = 850 mb and p_t is defined as the top of the optimal steering layer. The second subscripts "o" and "m" indicate the observed storm and CFSR steering flow and the model storm and steering flow, respectively. A small residual term as shown in Table 3 exists for (8) and (9) since the actual storm motion does not exactly equal the optimal steering flow, in most cases due to the influence of, for example, (i) storm-scale processes, (ii) the distribution of convection (in response to vertical wind shear) relative to the storm center, and (iii) uncertainties in the CFSR wind analysis, on storm motion.

Figure 3 shows the evolution of the environment of TC Earl during 27 August–4 September 2010. Note that prior to 0000 UTC 2 September the magnitude of the residual between the vector TC motion and the vector optimal steering flow was below 0.5 m s^{-1} regardless of the forward speed, deep-layer vertical wind shear, and intensity of TC Earl (Figs. 3a,b). The steering flow residual increased markedly during and after recurvature as TC Earl moved into a baroclinic environment with deep cold advection (Fig. 3c); a common signature for TCs as they recurve and transition into asymmetric baroclinic cyclones that propagate to the left of the expected motion based on the steering flow alone (e.g., Gray 1994).

Changes in optimal steering flow depth and radius can occur during the mature phase of a TC as illustrated by the time series for TC Earl (Fig. 3b). The optimal steering flow depth increased from 450 mb (850–400-mb layer) at 0000 UTC 27 August to 650 mb (850–200-mb layer) at 0000 UTC 29 August as TC Earl gradually intensified to a strong tropical storm. As TC Earl continued to intensify to a ~60 m s^{-1} TC by 0000 UTC 31 August, however, the optimal steering depth became shallower reaching 500 mb (850–350-mb layer). The reduction in optimal steering depth occurred as upper-tropospheric storm-relative northwesterlies developed in conjunction with the diffluent jet-exit region northwest of TC Earl (not shown). Since TC Earl was still moving toward the northwest at 0000 UTC 31 August, the automated algorithm selected a shallower steering layer that better matched the actual storm motion. The optimal steering flow radius varied between 3° and 4° through 0000 UTC 31 August. By 0000 UTC 2 September the optimal steering depth deepened back to 650 mb, which is consistent with well-developed TCs as described in previous work (e.g., Velden and Leslie 1991), as TC Earl recurved into midlatitudes (cf. Fig. 1). Additionally, the optimal steering flow radius decreased to 2° during recurvature (Fig. 3b). In general, the radius tends to decrease in situations where near-storm vorticity asymmetries associated with synoptic-scale weather systems is large. During recurvature, near-storm vorticity asymmetry—manifested as anticyclonic (cyclonic) vorticity to the east (west)—is

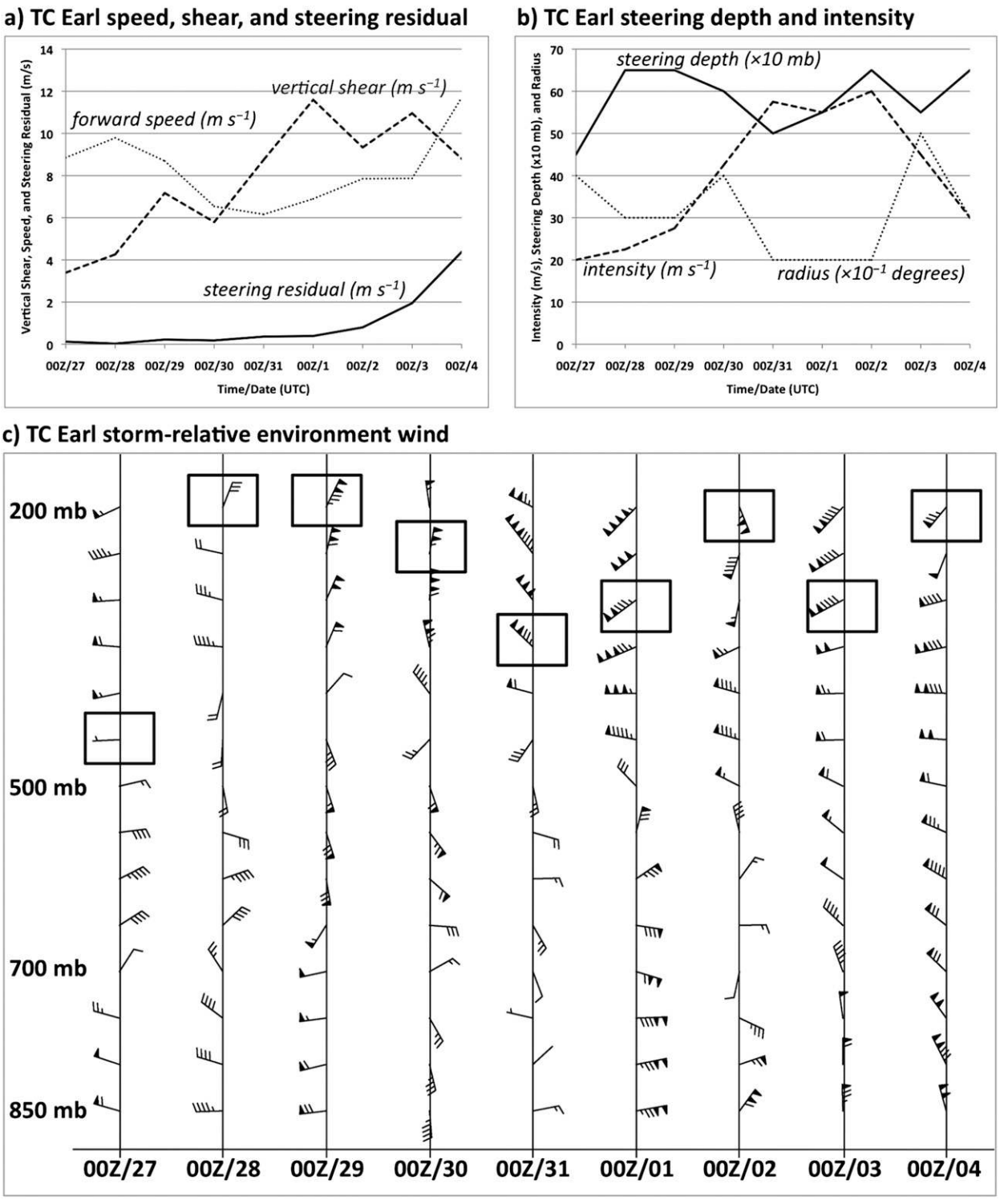

FIG. 3. Quasi-Lagrangian time series of (a) 850–200-mb vertical shear (dashed line in m s^{-1}), optimal steering flow vector residual error magnitude (solid line in m s^{-1}), and forward speed (dotted line in m s^{-1}) and (b) optimal steering depth (solid line in ×10 mb), radius (dotted line in $\times 10^{-1}$ degrees), and intensity (dashed line in m s^{-1}) every 24 h at 0000 UTC 27 Aug–4 Sep 2010 for TC Earl. (c) Vertical profile of TC-relative environment wind (half barb = 0.25 m s^{-1}; full barb = 0.50 m s^{-1}; pennant = 2.50 m s^{-1}) every 50 mb at 0000 UTC 27 Aug–4 Sep 2010 for TC Earl. The top of the optimal steering flow layer is indicated by the open square. The vertical shear was computed using a 5° TC removal radius, while the optimal steering flow error was computed using a variable TC removal radius as described in the text. All information was computed using the CFSR.

driven by the subtropical ridge to the east and the midlatitude trough to the west (not shown).

By 0000 UTC 1 September, the forward motion of TC Earl increased in response to strengthening and deepening storm-relative southwesterly flow (Fig. 3c) in conjunction with the approach of an upper-level trough from the west (not shown). In cases where the steering layer depth becomes shallower despite no evidence that the TC vortex has weakened or become shallower, there are typically several depth and radius combinations that have comparably small steering flow residual errors, contributing to an uncertainty in the optimal steering layer depth (radius) on the order of approximately ±50 mb (±1.0°). An additional factor that may contribute to changes in the optimal steering layer depth are the influence of the asymmetric distribution of convection in environments with increased vertical wind shear on storm motion (e.g., Wang and Holland 1996). The automated algorithm will select the optimal steering layer depth that best matches the actual storm motion regardless if the TC is simply being advected by the flow or is also propagating within the flow in response to convective processes.

c. Storm motion error diagnosis

We can use (6)–(9) to derive a diagnostic equation that quantitatively represents the sources for forecast TC motion error. The full derivation is provided in the appendix. If we define the actual TC motion error as $\mathbf{V}_m - \mathbf{V}_o$, then assuming that the steering layer residual error is small we can define the storm motion error diagnostic equation as

$$\underbrace{\mathbf{V}_m - \mathbf{V}_o}_{\text{storm motion error}} = \underbrace{\frac{1}{p_b - p_{t,o}} \int_{p_{t,o}}^{p_b} (\hat{\mathbf{v}}_m - \mathbf{v}_o)\, dp}_{\text{environment wind error}} + \underbrace{\frac{1}{p_b - p_{t,m}} \int_{p_{t,m}}^{p_b} -(\hat{\mathbf{v}}_m - \mathbf{v}_m)\, dp}_{\text{TC removal radius error}}$$
$$+ \underbrace{\frac{1}{p_b - p_{t,m}} \left[\int_{p_{t,o}}^{p_b} \left(\frac{p_{t,m} - p_{t,o}}{p_b - p_{t,o}} \right) \hat{\mathbf{v}}_m\, dp + \int_{p_{t,m}}^{p_{t,o}} \hat{\mathbf{v}}_m\, dp \right]}_{\text{TC steering depth error}} + \text{residual term}. \tag{10}$$

The first term on the right-hand side represents the contribution from model environment wind errors in the observed steering flow layer, the second term represents the contribution from differences in the TC removal radius between the model and observed TC in the model steering flow layer, and the third term represents the contribution from differences between the model and observed steering layer vertical depth. The fourth term represents the residual term, which includes analysis wind errors, storm motion errors introduced by uncertainties in TC position, and the steering residual in (8) and (9) (see also Table 3).

The environment wind error term in (10) is defined as the model environment wind minus the CFSR environment wind integrated over the steering depth for the observed storm, both using the radius defined for the observed storm. Thus, the environment wind error term is a function of only the difference in wind between the analysis and forecast all due to vorticity and divergence differences outside of r_o since it is this vorticity and divergence that drives the wind inside of r_o. Because the 24-h forecast position error is generally less than 150 km, and because the environment wind typically varies slowly across the disk from which the TC was removed, most of the environment wind error term is due to wind differences in physical space rather than differences in storm position. The use of a local coordinate system therefore does not affect the validity of the diagnostic calculation. In instances where the 24-h forecast position error is large, however, the increased environment wind error occurs because the TCs are in different environments altogether, which complicates the interpretation of the diagnostic equation. For this reason, we restrict our diagnostic analysis to 24-h model forecasts.

The next two terms in (10)—TC removal radius and vertical steering depth term—arise because we allow the radius and vertical steering depth to differ between the model and observed storm at a given time. In cases when $p_{t,m} = p_{t,o}$ or when $\hat{\mathbf{v}}_m(p)$ does not vary with pressure (no vertical shear) the steering depth term will go to 0. Likewise, when $r_m = r_o$ the radius term will go to 0. We will examine how the terms in the diagnostic equation (10) behave for two storms of interest from the AHW retrospective period—TCs Earl and Fiona—in sections 5 and 6.

3. Results from retrospective AHW TC motion forecasts

a. Deep-layer versus optimal layer steering

In considering the TC motion that results from the vertically integrated environment wind over the steering

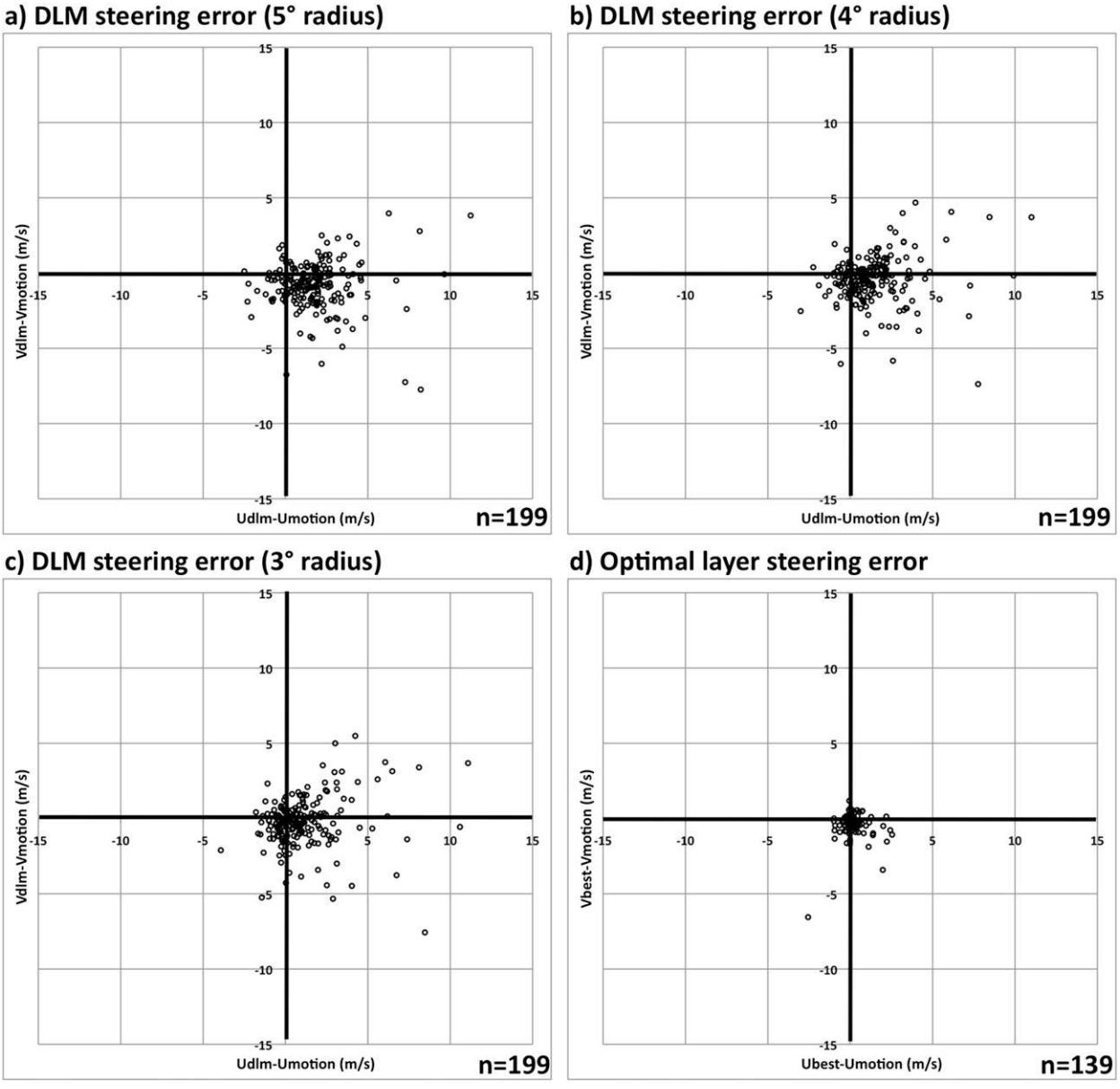

FIG. 4. The observed steering residual error (steering vector − storm motion vector) in u and v space (m s^{-1}) at 0000 UTC for all North Atlantic TCs included in the AHW retrospective period of 2008–10 (199 data points over 27 storms) for the DLM steering using a TC removal radius of (a) 5°, (b) 4°, and (c) 3°, and (d) optimal layer steering. The optimal layer steering residual error was computed only for those storms in which there were corresponding AHW forecasts (139 data points over 27 storms). The steering was computed using the CFSR and the storm motion was computed by using the HURDAT positions at ±12 h.

layer, we will now examine and compare the utility of using the DLM (defined here at the 850–200-mb layer) steering flow versus the optimal layer steering flow as described in section 2b for observed storms during the AHW retrospective period (Table 2). For the computation of the DLM steering flow, a fixed radius of 5° was used to be consistent with previous papers that removed the TC vortex prior to computing steering or vertical shear (e.g., Corbosiero and Molinari 2002). Although the DLM steering flow has a strong correlation (>0.8; not shown) with the actual storm motion, there is a distinct east-southeastward bias with a mean vector residual [computed from (8)] magnitude of 1.97 m s^{-1} (Fig. 4a and Table 4).

The southeastward bias associated with the DLM steering flow is likely due to underrepresentation of

TABLE 4. The mean observed residual error of the DLM steering flow defined using a 5°, 4°, and 3° TC removal radii, and the optimal steering flow using the optimal TC removal radii for all TCs during the AHW retrospective period (2008–10). The TC motion is defined using the best track positions at ±12 h and the steering flow is defined using the CFSR.

Depth	Radius	u error (m s^{-1})	v error (m s^{-1})	Magnitude (m s^{-1})
DLM	5°	1.78	−0.84	1.97
DLM	4°	1.45	−0.41	1.51
DLM	3°	1.15	−0.23	1.18
Optimal	Optimal	0.17	−0.26	0.31

southeasterly flow driven by potential vorticity (PV) anomalies associated with the beta effect (e.g., Fiorino and Elsberry 1989). Shapiro and Franklin (1995) showed using observations of TC Gloria (1985) that the PV anomalies associated with the beta effect are located almost completely within the 5° TC removal radius used herein for the DLM steering calculation. Reducing the TC removal radius to 4° and 3° lessens the southeastward bias by nearly 1.0 m s^{-1}, confirming that the relatively large southeastward steering residual is likely due to the removal of the beta gyres (Figs. 4b,c and Table 4). Note, however, that the smaller TC removal radii do not reduce the fairly large scatter in the distribution, which makes quantitative diagnostic analysis difficult.

The optimal steering flow substantially reduced the southeastward steering flow bias and the scatter in the distribution compared to the DLM steering (Fig. 4d). This improvement in the agreement between TC motion and steering flow, with the mean magnitude of the vector residual reduced to 0.31 m s^{-1} (Table 4), is not surprising since the optimal steering layer method searches for the steering flow that best matches the actual storm motion. The optimal steering flow also improves the agreement between steering flow and TC motion in environments with large vertical shear (not shown). The key result here is that while the DLM steering flow method corresponds well with TC motion, the optimal steering flow method used herein reduces the steering flow residual, and allows for a quantitative diagnostic analysis of the sources of errors in forecast TC motion.

A statistical overview of optimal TC removal radius and steering depth for all 0-h CFSR and 24-h AHW forecasts from the 2008–10 North Atlantic TC seasons is shown in Fig. 5. The deepest steering-layer depths are most common across the entire range of TC removal radii in both the 0-h CFSR forecasts and AHW 24-h forecasts (Figs. 5a,b). The 0-h CFSR and 24-h AHW depth distributions are not significantly different as computed using the nonparametric Wilcoxon–Mann–Whitney rank sum test (Wilks 1995, 138–143).[5] Note, however, that while deep and medium steering layer depths occur most commonly with 3°–4° TC removal radii in both the 0-h CFSR and 24-h AHW forecasts, shallow steering layer depths occur preferentially at larger TC removal radii in the CFSR (Figs. 5c,d); a signature that is significant at the 99% level. The tendency for the CFSR to prefer larger radii is likely a reflection of the effect of increased vertical shear to reduce the depth of the vortex and broaden the wind field; a common signature of vertically sheared TCs in an increasingly baroclinic environment (e.g., Gray 1994). The preference for large radii at shallow steering layer depths is not as prevalent for TCs in AHW (cf. Figs. 5c,d), and suggests that structure of TCs in vertical shear differs between AHW and the CFSR. The behavior of TCs in a vertically sheared environment will be discussed further in section 3b. Additionally, the overall preference for larger radii in the CFSR compared to AHW suggests that the TC environment wind in the CFSR is driven primarily by synoptic-scale weather systems, while in AHW it is also influenced by near-storm vorticity asymmetries. How differences in TC removal radii may affect storm motion will be discussed further in section 5.

b. *Statistical overview of the storm motion error diagnostic*

This subsection provides a statistical overview of the TC motion error diagnostic equation for 24-h AHW forecasts from the 2008–10 North Atlantic seasons as described in section 2. The TC motion error computations were stratified by the direction of motion of the observed TC into westward (240°–300° direction of motion), northwestward (300°–360°), and northeastward (0°–60°) TC motion. Furthermore, the westward- and northwestward-moving TCs were stratified by their location in the North Atlantic basin defined as either west or east of 60°W. The longitude of 60°W was chosen because manual inspection of synoptic charts from the 2008–10 North Atlantic seasons showed that, in general, TCs east of 60°W were steered primarily by the subtropical ridge, while TCs west of 60°W had a more frequent additional influence on steering flow from midlatitude troughs.

Figure 6 shows the vector magnitude of the storm motion error diagnostic equation terms and the CFSR 850–200-mb vertical shear for all 2008–10 North Atlantic TCs stratified by the observed TC motion and location.

[5] The Wilcoxon–Mann–Whitney rank sum test is used for all significance testing unless otherwise noted.

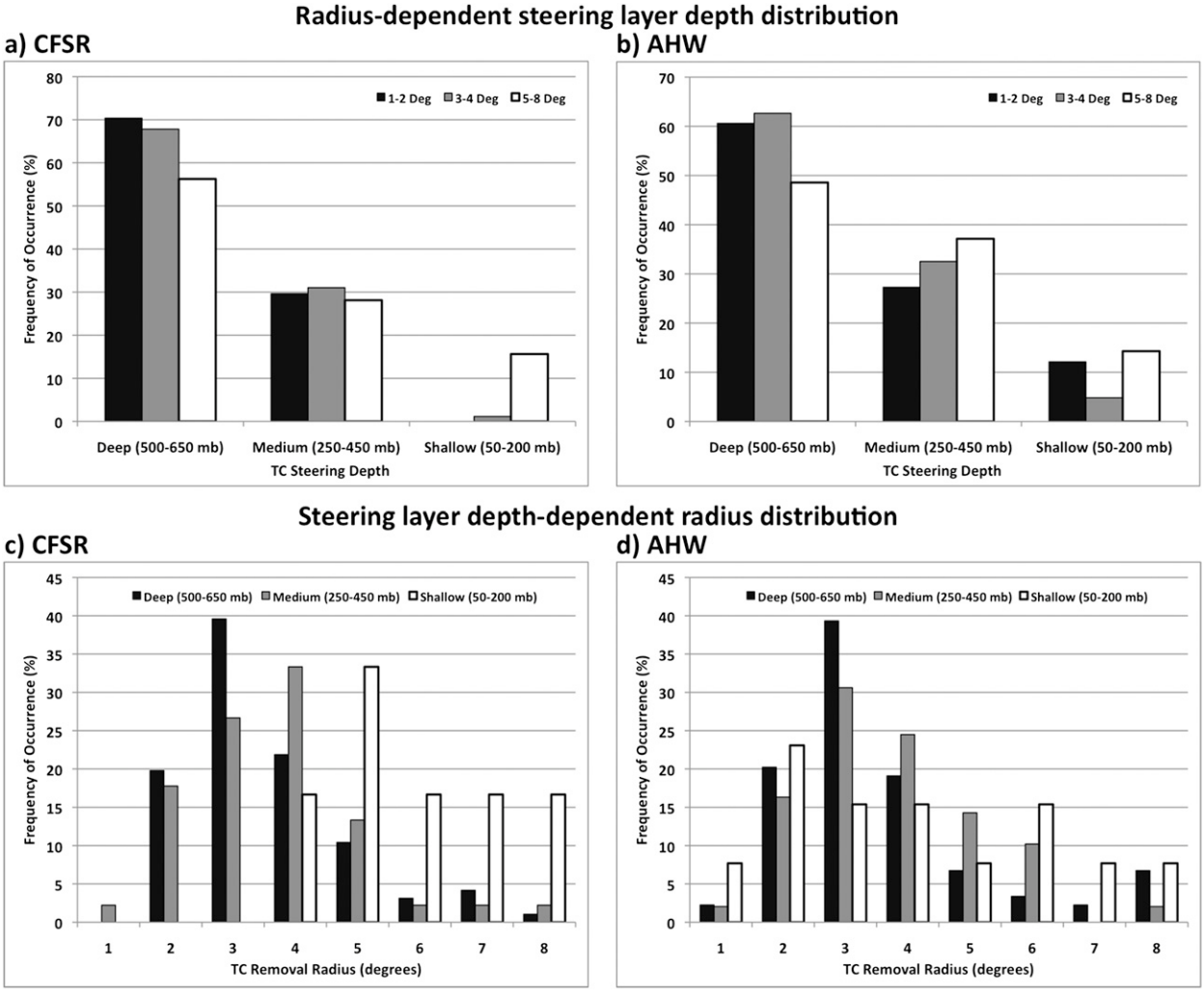

FIG. 5. Histogram of optimal steering layer depth for 1°–2° (black), 3°–4° (gray), and 5°–8° (white) TC removal radii for (a) 0-h CFSR and (b) 24-h AHW forecasts, and of optimal TC removal radius for deep (black), medium (gray), and shallow (white) optimal steering layer depths for (c) 0-h CFSR and (d) 24-h AHW forecasts for all TCs during the AHW retrospective period. Deep, medium, and shallow steering layer depths correspond to depths of 500–650, 250–450, and 50–200 mb, respectively.

For the terms on the right-hand side of (10), only the $\mathbf{v}_{\text{env}}$ error term (median values ranging from 1.0–1.7 m s^{-1}) was significantly larger than the residual error term at the 99% level for each of the motion and location categories (Figs. 6a–e). The $\mathbf{v}_{\text{env}}$ error term is larger than the radius and depth error terms 69% and 81% of the time for all TCs, respectively (not shown). Only the $\mathbf{v}_{\text{env}}$ error for westward-moving TCs east of 60°W was systematic in direction, showing an eastward $\mathbf{v}_{\text{env}}$ error that contributed to a slow bias in the forecasted TC motion (not shown). The TC removal radius error term for westward-moving TCs west of 60°W was weakly significant at the 90% level compared to the residual error (Fig. 6a), but was not systematic in direction (not shown). The TC removal radius and steering layer depth error terms are not significantly larger than the residual term for all other motion and location categories. This result shows that only the $\mathbf{v}_{\text{env}}$ error is systematic and robust in AHW (Figs. 6a–e). While the radius and depth error terms do not have a significant long-term signal relative to the residual error term on average over several seasons, these terms can dominate the residual term at individual forecast times.

The vector magnitude 850–200-mb vertical shear was lowest for westward-moving TCs east of 60°W, while the other motion categories are significantly larger at the 99% level (Fig. 6f). The vector magnitude of the residual error is larger for TCs embedded in larger 850–200-mb vertical wind shear, with the largest residual error and vertical wind shear occurring with northeastward-moving TCs. In general, the TC motion errors for all TCs

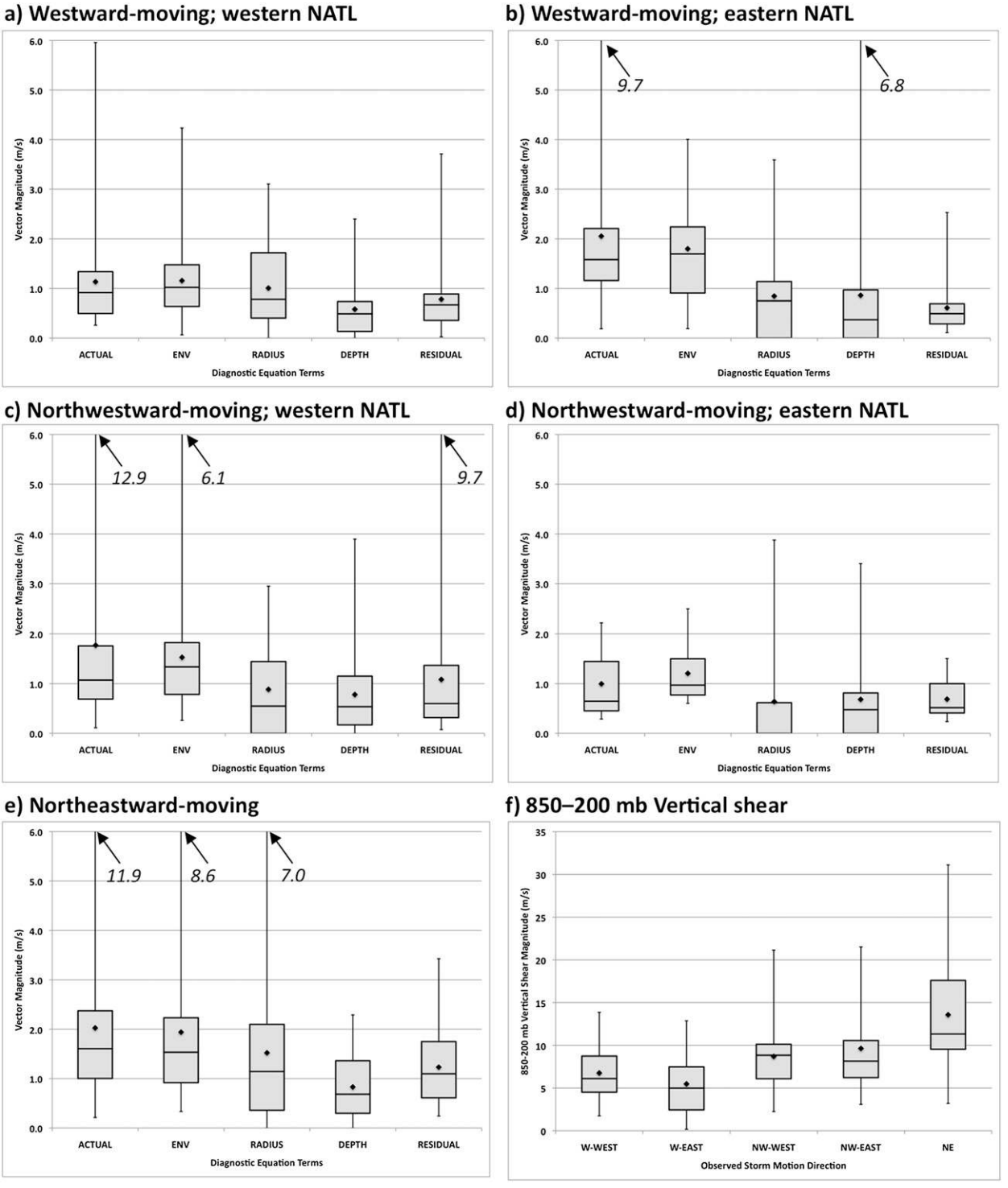

FIG. 6. Box-and-whisker diagram of the vector magnitude (m s^{-1}) of all the terms in the motion error diagnostic equation shown in (10) for (a) westward-moving TCs located west of 60°W, (b) westward-moving TCs located east of 60°W, (c) northwestward-moving TCs located west of 60°W, (d) northwestward-moving TCs located east of 60°W, and (e) northeastward-moving TCs over the entire North Atlantic. The terms were computed for TCs during the 2008–10 AHW retrospective period. (f) The vector magnitude of the 0-h CFSR forecast 850–200-mb vertical wind shear for westward-moving TCs located west of 60°W, westward-moving TCs located east of 60°W, northwestward-moving TCs located west of 60°W, northwestward-moving TCs located east of 60°W, and northeastward-moving TCs over the entire North Atlantic. The lower (upper) bound of the box marks the 25th (75th) percentile, and the horizontal black line in the box marks the median value. The whiskers mark the maximum and minimum value, and the diamond marks the mean value.

TABLE 5. The frequency of negative values from the vector dot product of TC motion error and CFSR-derived 850–200-mb vertical wind shear for the observed TC during the AHW retrospective period.

Direction of motion	TC location	Percent < 0 (%)
Westward	West of 60°W	61
Westward	East of 60°W	56
Northwestward	West of 60°W	56
Northwestward	East of 60°W	21

except northwestward-moving TCs east of 60°W tend to be in the opposite direction compared to the 850–200-mb vertical shear as summarized in Table 5. Balanced motions associated with a vortex embedded in vertical shear favors the development of convection downshear of the vortex center (e.g., Raymond and Jiang 1990). This asymmetric distribution of convection will contribute to TC motion in the downshear direction by generating positive PV at low levels in conjunction with diabatic heating at mid- and upper levels. That the motion error in the 24-h AHW forecasts tends to be in the upshear direction suggests that the distribution of convection in TCs embedded in vertical shear may be too symmetric. Investigating the influence of convection on TC motion, and whether the convection for vertically sheared storms in AHW is too symmetric, is the subject of ongoing research.

4. Overview of TCs Earl (2010) and Fiona (2010)

The 24-h AHW forecast motion errors for TC Earl and Fiona will now be examined quantitatively to highlight the rich complexity and physical processes that are driving the systematic AHW forecasted TC motion errors described previously. This section briefly describes the synoptic-scale environment in which these TCs were embedded by using the CFSR analysis of 200-mb PV, wind, and 850-mb relative vorticity shown in Fig. 7. Discussions of the life cycles of TCs Earl and Fiona can also be found in Cangialosi (2011) and Berg (2010), respectively.

During the last week of August and first week of September 2010, TCs Danielle, Earl, Fiona, and Gaston developed from African easterly waves and moved westward over the North Atlantic main development region. During 27–29 August, TC Danielle moved northwestward over the western North Atlantic while TC Earl and the pre-Fiona tropical disturbance moved westward south of 20°N (not shown). By 0000 UTC 29 August, TC Danielle recurved into midlatitudes in advance of an upper-level trough just off the U.S. East Coast (Fig. 7a). Amplification of the flow over and eastward of TC Danielle contributed to trough deepening north of TC Earl. Tropical cyclone Earl underwent rapid intensification as it moved into the base of the ridge that formed in conjunction with Danielle's recurvature at 0000 UTC 31 August (not shown). At the same time, TC Fiona was located near 50°W on the eastern flank of the upper-level trough that interacted with TC Earl previously. By 0000 UTC 2 September, TC Earl recurved into midlatitudes in response to an approaching midlatitude trough over the eastern United States. At the same time, TC Fiona moved northwestward beneath TC Earl's outflow anticyclone (Fig. 7b).

Tropical cyclone Gaston followed a track similar as the three previous TCs discussed above while east of 50°W (Fig. 7b), but was not able to sustain TC strength and stayed on a westward course into the Caribbean Sea after 2 September (not shown). In all, the period considered here featured numerous TCs being influenced by several flow features originating from midlatitudes and influencing each other. This provides a rich variation of environmental flows and TC intensity and structure. The next two sections will examine the AHW forecasts of TCs Earl and Fiona (Fig. 1), and quantitatively diagnose and physically explain the sources of forecast motion errors for selected AHW forecasts for both TCs.

5. TC Earl (2010) errors

The decomposition of the 24-h AHW forecast motion errors verifying at 0000 UTC 27 August–1 September 2010 for TC Earl is presented in Fig. 8a (see also Table 6).[6,7] The TC motion error for each 24-h AHW forecast is generally eastward, or "slow," since the actual TC motion has a westward component throughout the period shown. The slow forecast motion error is driven primarily by an eastward environment wind error in the steering layer. Errors in the vertical depth of the steering layer and the TC removal radius are generally smaller, but are occasionally as large as errors in environment flow. The 24-h AHW forecasts verifying at 0000 UTC 27, 29, and 31 August will now be examined in more detail to help illustrate how one can interpret the physical reasoning behind the individual terms in the motion error diagnostic.

[6] The CFSR and AHW steering depth, radius, and residual error for the forecasts of TCs Earl and Fiona presented herein are summarized in Table 6.

[7] Computation of the storm motion error diagnostic for AHW against the Interim ECMWF Re-Analysis (ERA-I; Dee et al. 2011) yielded similar results, with average differences in magnitude between CFSR and ERA-I of $\sim$0.2 m s^{-1} for the residual term and $\leq$0.1 m s^{-1} for each remaining diagnostic term.

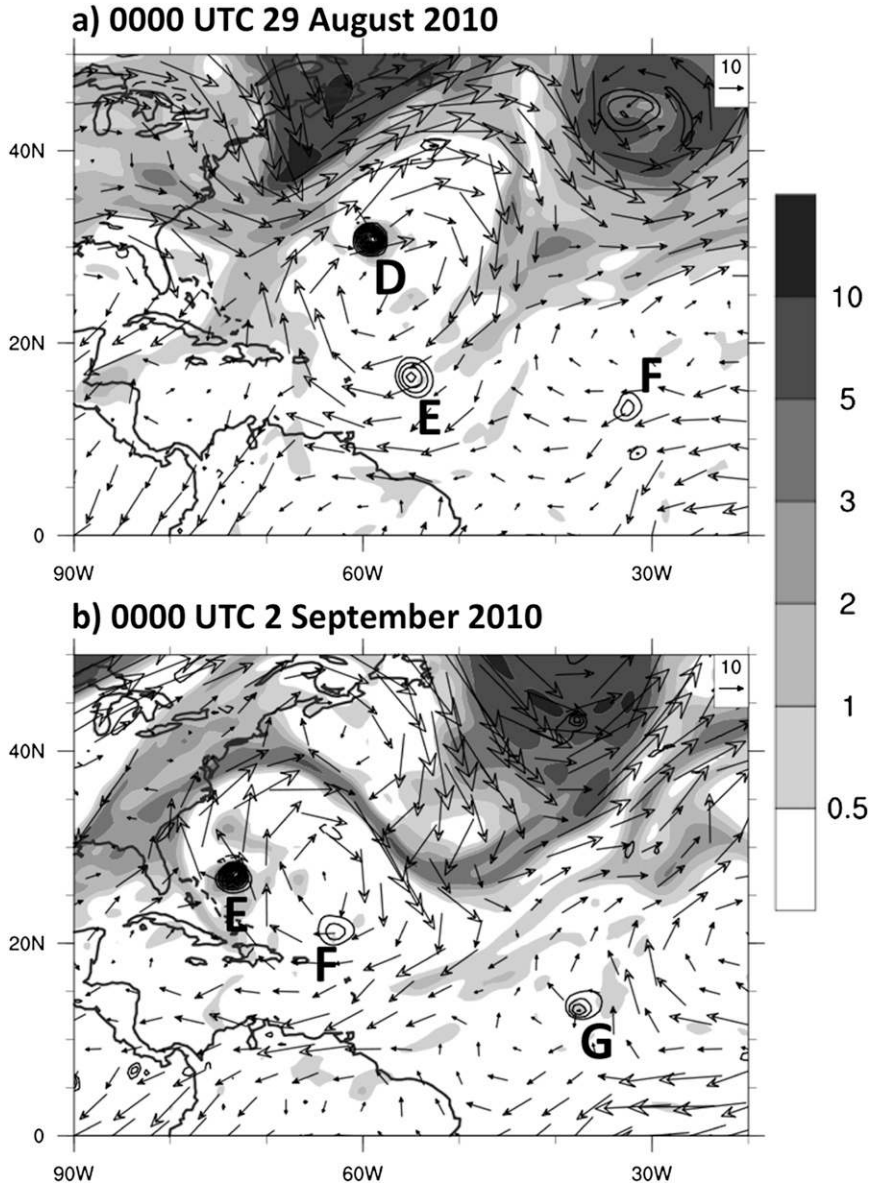

FIG. 7. CFSR 200-mb potential vorticity [shaded according to the grayscale in potential vorticity units (PVU; 1.0 PVU = 1.0×10^{-6} m^2 s^{-1} K kg^{-1}), wind (arrows in m s^{-1}), and 850-mb relative vorticity (solid contours every 8.0×10^{-5} s^{-1} starting at 8.0×10^{-5} s^{-1}) at 0000 UTC (a) 29 Aug and (b) 2 Sep 2010. TCs Danielle, Earl, Fiona, and Gaston are labeled D, E, F, and G, respectively.

The 24-h AHW forecast verifying at 0000 UTC 27 August indicates a 4.3 m s^{-1} east-southeastward error in TC motion, driven primarily by a 3.1 m s^{-1} eastward error contribution from the environment wind and by a 1.4 m s^{-1} southeastward error contribution from the vertical depth (Fig. 8a). In all, these errors contributed to a slow forecast error in storm motion. The errors in the environment wind in the steering layer—the primary source of TC motion error in this 24-h AHW forecast—is illustrated by the vertical profile of environment flow for TC Earl (Fig. 9a). The vertical profile shows that the 24-h AHW forecast had anomalous west-southwesterly flow throughout the observed steering layer, resulting in the eastward environment wind error in Fig. 8a. The environment wind error $[\mathbf{v}_{\mathrm{ahw}}(x, y, p) - \mathbf{v}_{\mathrm{obs}}(x, y, p)]$ vertically integrated in the observed steering layer with TC Earl removed shows a broad region of eastward wind error south of a cyclonic anomaly north-northwest of

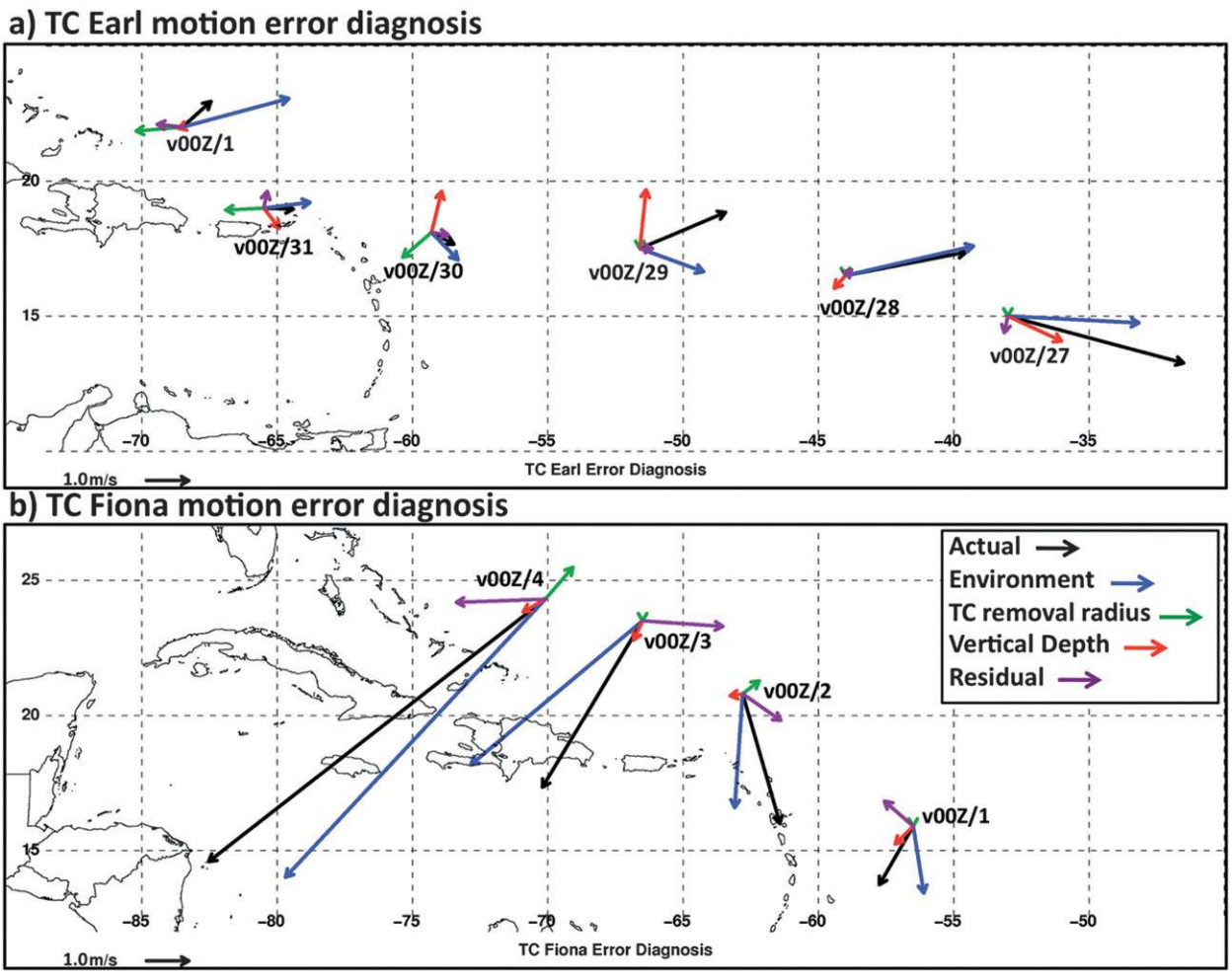

FIG. 8. The TC motion error diagnostic equation terms (m s^{-1}; reference vector is plotted on the bottom left of both panels) for AHW 24-h forecasts of (a) TC Earl and (b) TC Fiona. The 24-h forecasts shown for TC Earl verify at 0000 UTC 27 Aug–1 Sep 2010, and for TC Fiona at 0000 UTC 1–4 Sep 2010. The key on the top-right part of (b) shows the arrow color for each term in the motion error diagnostic equation.

TC Earl at 0000 UTC 27 August (Fig. 10a). The cyclonic wind anomaly and eastward wind error was associated with a broad region of negative 600-mb geopotential height error throughout the subtropics north of TC Earl (Fig. 10b), illustrating how the 24-h AHW forecast poorly represented the intensity of the subtropical ridge, which contributed to tropical easterlies that were too weak on the equatorward flank of the ridge.

TABLE 6. The 0-h forecast CFSR and 24-h forecast AHW steering layer depth (mb), radius (°), and steering residual error (m s^{-1}) for TCs Earl and Fiona. Verification date–time is year 2010 and 0000 UTC in all cases.

Storm	Verification date–time	CFSR depth (mb)	CFSR radius (°)	CFSR residual error (m s^{-1})	AHW depth (mb)	AHW radius (°)	AHW residual error (m s^{-1})
Earl	27 Aug	450	4	0.49	200	4	0.12
	28 Aug	650	3	0.15	300	3	0.03
	29 Aug	650	3	0.16	500	3	0.22
	30 Aug	600	4	0.34	500	2	0.18
	31 Aug	500	4	0.35	550	2	0.36
	01 Sep	550	2	0.32	650	3	0.39
Fiona	01 Sep	650	3	0.12	500	3	0.79
	02 Sep	550	3	1.75	600	4	0.72
	03 Sep	450	3	2.47	500	3	1.83
	04 Sep	350	2	1.58	400	3	1.40

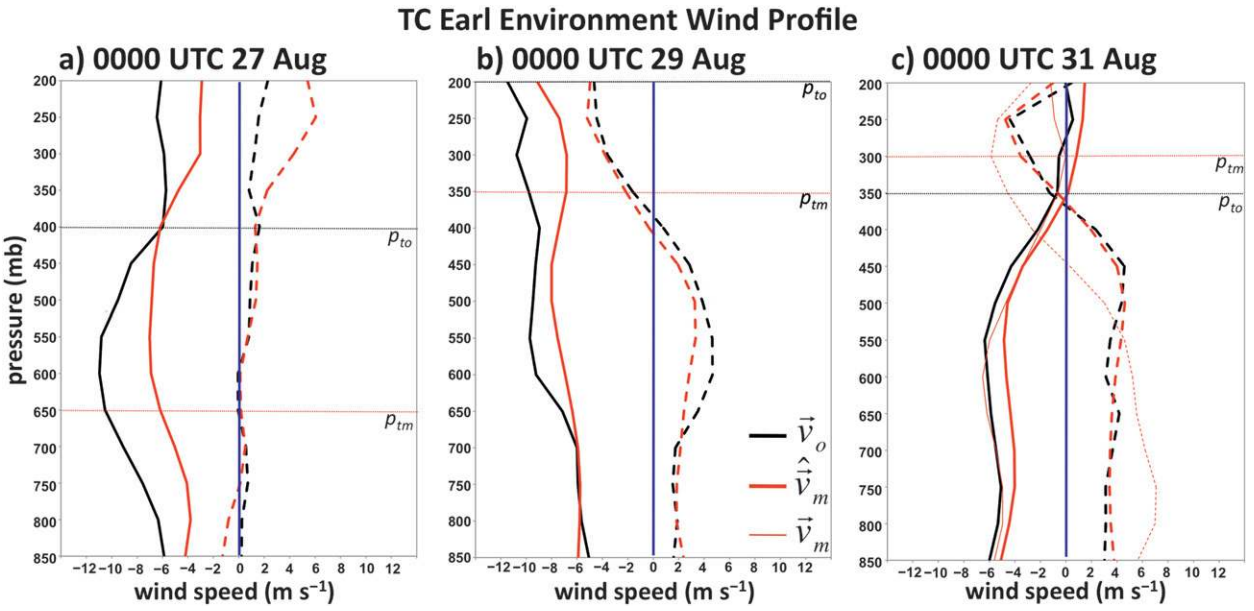

FIG. 9. Vertical profile of TC Earl's environment wind (m s^{-1}) for the 0-h CFSR forecast (black line) and 24-h AHW forecast (red lines) both verifying at 0000 UTC (a) 27, (b) 29, and (c) 31 Aug 2010. The thick black lines, thick red lines, and thin red lines represent $\mathbf{v}_o$, $\hat{\mathbf{v}}_m$, and $\mathbf{v}_m$, respectively. Thin red lines are not plotted in (a) and (b) because $r_m = r_o$. The u -wind component is plotted using solid lines and v -wind component dashed lines. The horizontal dotted black (red) line marks the top of the optimal steering layer for the 0-h CFSR (24-h AHW) forecast. The zero contour is marked by the vertical blue line.

The southeastward contribution to TC motion error from the vertical depth error term arises because the observed TC responded to a deeper steering layer than did the 24-h AHW forecast TC (Fig. 9a). The AHW environment wind due to differences in optimal steering layer depth, $\mathbf{v}_{\text{ahw}}(x, y, p)$, vertically integrated in the layer between $p_{t,m}$ and $p_{t,o}$, shows a broad region of southeasterly flow error over TC Earl at 0000 UTC 27 August (Fig. 11a). Because the model TC was steered by a shallower depth (850–650 mb) than the observed TC (850–400 mb), the southeasterly flow on the eastern flank of the upper-level trough west of TC Earl did not contribute to the motion of the AHW TC (Fig. 11b; see also Fig. 7a). Hence, the vertical depth error term shows a southeastward-directed error. The difference in vertical steering depth between the model and observed TC was likely due to the weaker and somewhat shallower AHW TC vortex compared to the observed TC as represented by the CFSR (Fig. 12a).

The 24-h AHW forecast of TC Earl verifying at 0000 UTC 29 August continued to show an eastward component to the motion error as in previous forecasts, although weaker with total error of 2.2 m s^{-1} comprising a southeastward environment wind error of 1.6 m s^{-1} and a north-northeastward vertical depth error of 1.4 m s^{-1} (Fig. 8a). The southeastward environment wind error through a deep layer (Fig. 9b) was associated with cyclonic flow around the base of the upper-level trough and anomalous westerly flow associated with a weaker subtropical ridge now northeast of TC Earl (Figs. 10c,d). The north-northeastward vertical depth error was associated with northerly flow between the upper-level trough to the northeast and the base of the upper-level ridge to the northwest (Figs. 11c,d). The AHW storm responded to a shallower steering layer (Fig. 9b) likely because it was weaker than the observed TC (Fig. 12b); hence, the northerly flow illustrated in Fig. 11c did not influence the model TC motion and contributed to a north-northeastward motion error.

Consistent with previous forecasts, the 24-h AHW forecast of TC Earl verifying at 0000 UTC 31 August shows an eastward motion error, albeit at a lesser magnitude compared to previous forecasts with total error of 0.7 m s^{-1} (Fig. 8a). In this case, an east-northeastward environment wind error of 1.1 m s^{-1} is balanced by a vertical depth error of 0.6 m s^{-1} pointing toward the southeast, a radius error of 0.9 m s^{-1} pointing toward the west-southwest, and a residual error of 0.4 m s^{-1} pointing toward the northwest. The northeastward environment wind error was driven in part by deep southwesterly flow associated with a cyclonic environment wind anomaly northwest of TC Earl (Figs. 9c and 10e). The cyclonic wind anomaly was associated with a negative 600-mb geopotential height error northwest

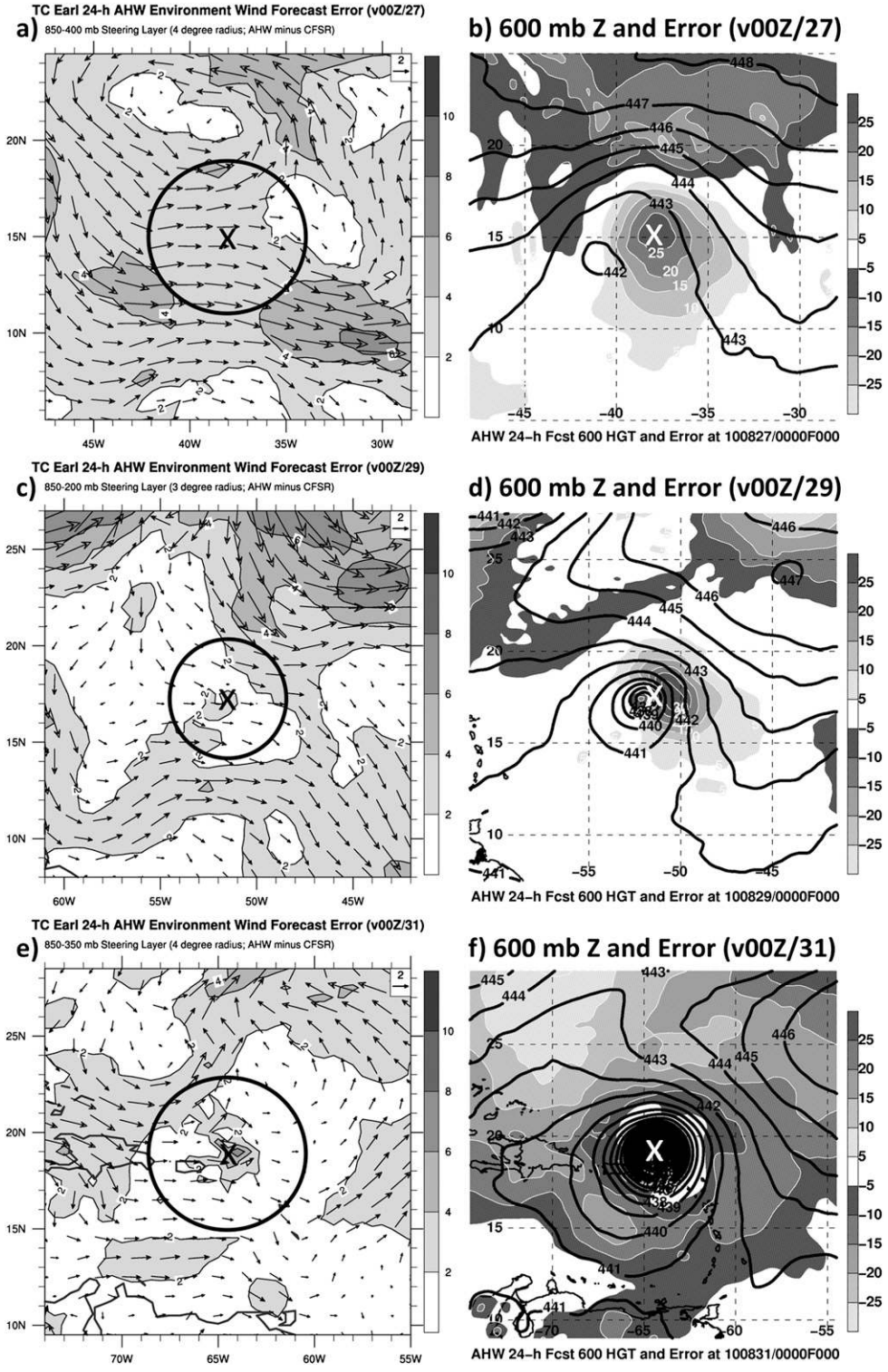

FIG. 10. AHW 24-h forecast environment wind vector error (AHW − CFSR; arrows with magnitude shaded with contours according to the grayscale in m s^{-1}) vertically averaged in the observed optimal steering layer verifying at 0000 UTC (a) 27, (c) 29, and (e) 31 Aug 2010. AHW 24-h forecast 600-mb geopotential height (solid contours every 1 dam) and height error (AHW − CFSR; shaded according to the grayscale in m) verifying at 0000 UTC (b) 27, (d), 29, and (f) 31 Aug 2010. The grids are shifted so the forecast and observed TC are located at the same position marked "X." The radius of TC removal is marked by the range rings on the left panels.

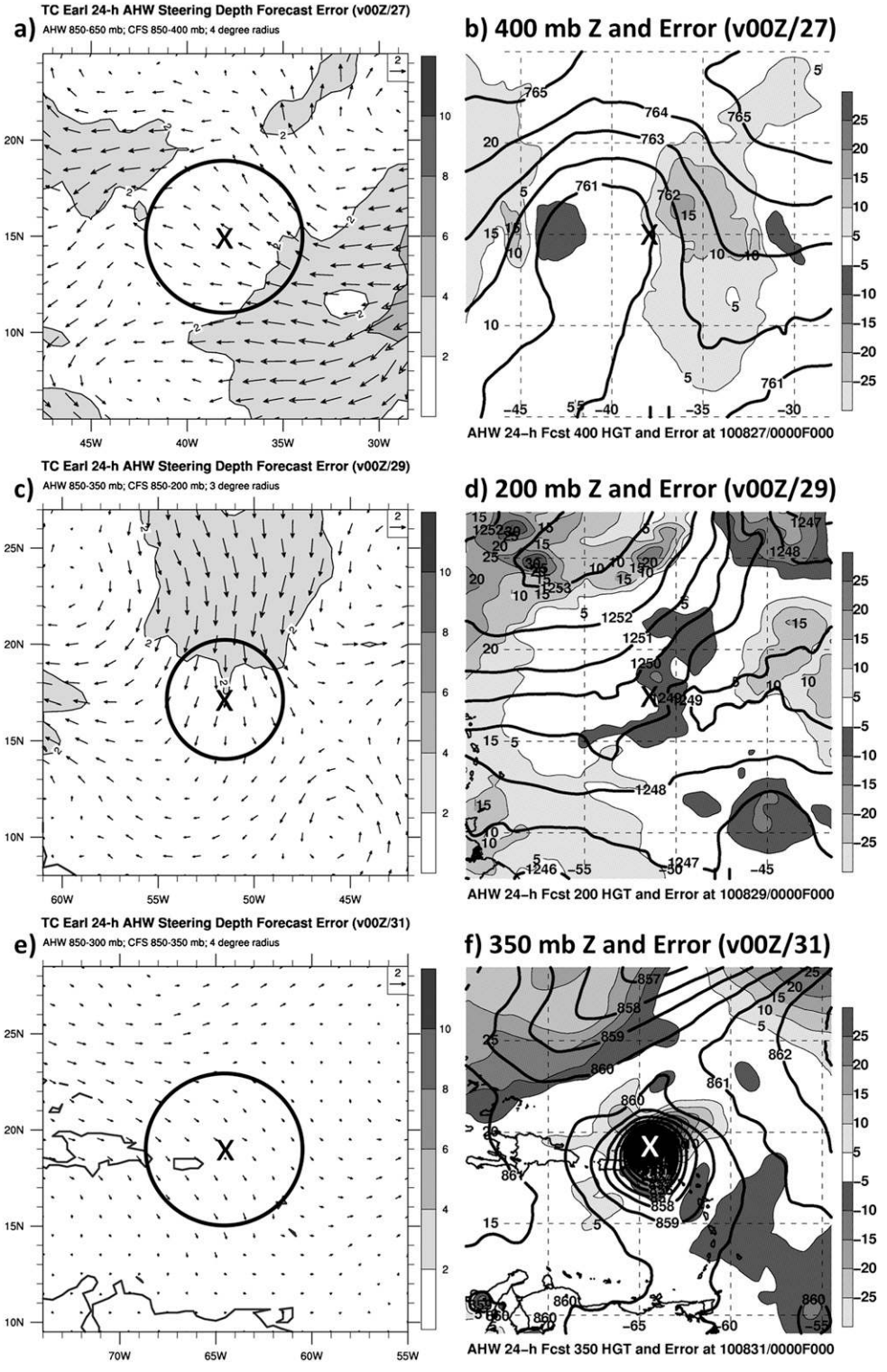

FIG. 11. AHW 24-h forecast environment wind vector error (arrows with magnitude shaded with contours according to the grayscale in m s^{-1}) vertically averaged in the layer between $p_{t,m}$ and $p_{t,o}$ verifying at 0000 UTC (a) 27, (c) 29, and (e) 31 Aug 2010. AHW 24-h forecast (b) 400-, (d) 200-, and (f) 350-mb geopotential height (solid contours every 1 dam) and height error (AHW − CFSR; shaded according to the grayscale in m) verifying at 0000 UTC (b) 27, (d), 29, and (f) 31 Aug 2010. The TC Earl is located at the position marked "X."

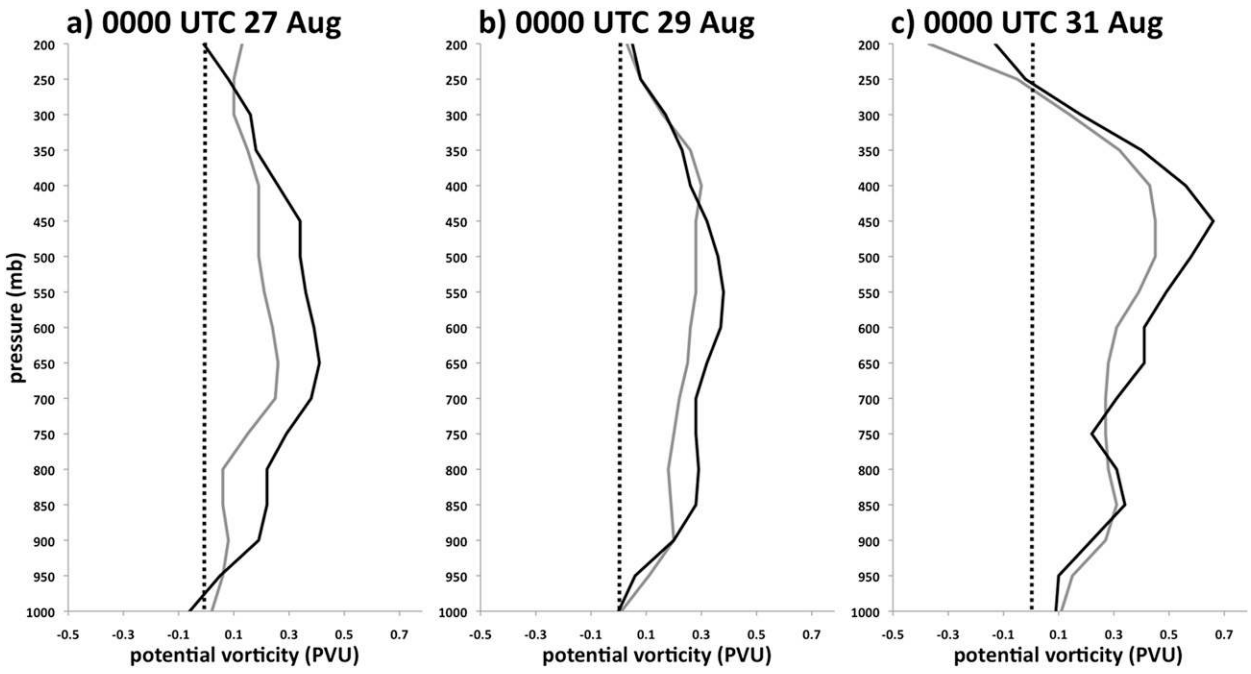

FIG. 12. Vertical profile of potential vorticity perturbation (PVU) verifying at 0000 UTC (a) 27, (b) 29, and (c) 31 Aug 2010 for TC Earl. The perturbation is defined as the 1.0° × 1.0° area-average potential vorticity − the 20.0° × 20.0° area-average potential vorticity. The gray (black) lines indicate the 24-h AHW (0-h CFSR) forecast.

of TC Earl (Fig. 10f), indicating that the 24-h AHW forecast had errors associated with the structure of the subtropical ridge north of TC Earl. The model TC was steered by a slightly deeper layer (850–300 mb) compared to observed (850–350 mb) (Fig. 9c and Table 6), which facilitated steering of TC Earl by the northwesterly flow aloft associated with the diffluent jet-exit region east of the upper-level trough to the northwest of TC Earl (Figs. 11e,f). Note, however, that the magnitude of the steering depth error is comparable to the residual error term and the 50-mb depth error is within the uncertainty bounds of the steering depth calculation, which is consistent with the similar vertical structure seen in both the CFSR analysis and AHW forecast (Fig. 12c).

The TC removal radius error occurs because the radius is larger for the observed TC compared to the AHW TC (4° vs 2°). The difference in radius contributed to a westward wind over the TC center (Fig. 13), and it appears that the difference in radius is related to (i) the much broader and elongated vortex ''skirt'' in the CFSR (supported by dropsonde observations) compared to the more compact model vortex, and (ii) the structure and coverage of the anticyclonic vorticity on the north side of the vortex, which contributed to well-defined near-storm vorticity asymmetry (Fig. 14). The more abundant anticyclonic vorticity that extended farther northwest on the north side of the observed vortex may be related to the more robust subtropical ridge in the CFSR compared to AHW. The net westward motion component in AHW compared to observations occurred because of vorticity asymmetries in the ring between 2° and 4° (Fig. 15). With the smaller radius for the AHW TC, the anticyclonic vorticity in the ring is not removed; hence, it becomes part of the environment wind steering the TC westward. With the observed optimal radius, this anticyclonic vorticity is removed. This easterly flow associated with the difference in radius counteracted the environment wind error term and yielded a small overall motion error because of canceling effects.

6. TC Fiona (2010) errors

The decomposition of the 24-h AHW forecast motion errors verifying at 0000 UTC 1–4 September 2010 for TC Fiona is presented in Fig. 8b. Storm motion errors were directed toward the south and southwest for all of the 24-h AHW forecasts initialized at 0000 UTC, with errors increasing in magnitude with each subsequent forecast. Environment wind errors dominate the overall forecast errors, with relatively smaller vertical steering depth and radius errors contributing to the total error. The large storm motion errors in the 24-h AHW forecasts led to remarkably poor TC position forecasts, with each

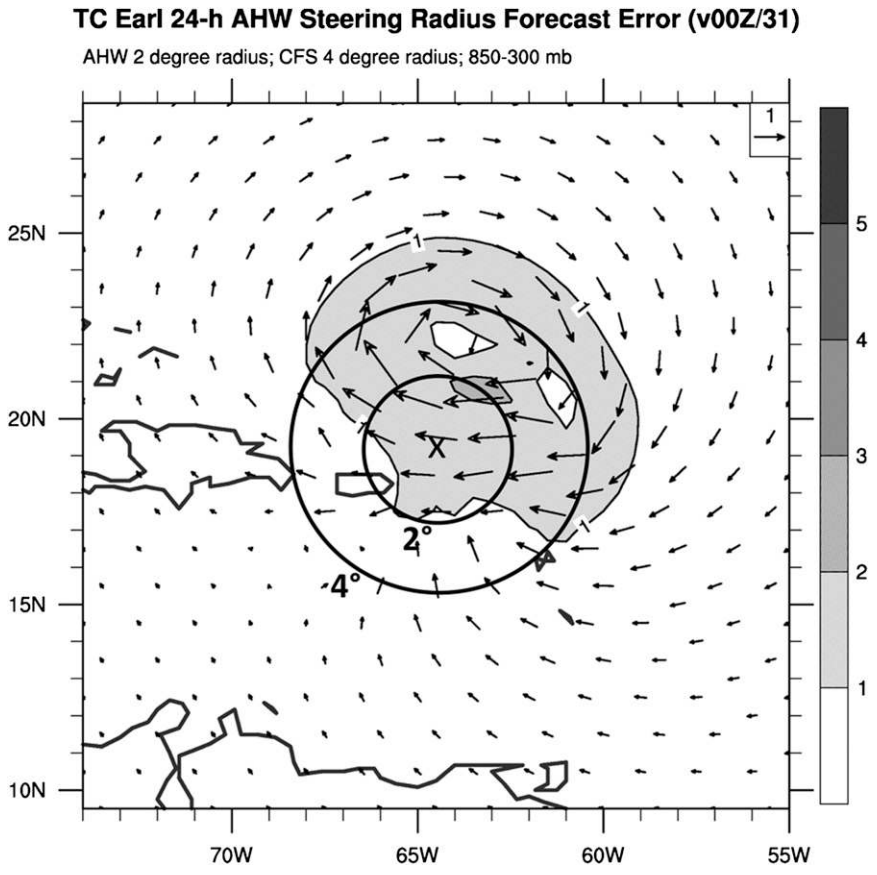

FIG. 13. AHW 24-h forecast environment wind error (arrows with magnitude shaded with contours according to the grayscale in m s^{-1}) vertically averaged in the AHW steering layer as a result of the use of different radii verifying at 0000 UTC 31 Aug 2010. The TC position is marked ''X.'' The radius of TC removal is marked by the range rings.

forecast failing to recurve TC Fiona into midlatitudes and instead moving TC Fiona due west toward the Gulf of Mexico (Fig. 1b).

Since the 24-h AHW forecast verifying at 0000 UTC 2 September is representative of the type of environment wind errors that occurred for all of the TC Fiona forecasts, we will examine this AHW forecast only. The AHW forecast reveals that the south-southeastward TC motion error of 3.2 m s^{-1} was largely due to the southward meridional environment wind error of 2.7 m s^{-1} averaged over the observed steering layer (Fig. 15). The southward environment wind error occurred over a large region between recurving TC Earl located northwest of TC Fiona and the subtropical ridge to the northeast of TC Fiona (Fig. 16a) and appears to be associated with the negative 700-mb geopotential height error northeast of TC Fiona (Fig. 16b). This error in the subtropical ridge—also documented with TC Earl—is a common signature in the 2011 version of the AHW. The ''plume'' of negative height error in the subtropical ridge appears to be a data assimilation problem, as it is apparent in the AHW analysis fields as early as 0000 UTC 31 August (Fig. 17a). The plume of negative 700-mb geopotential height error progressed westward with the flow north of TC Fiona, and was centered near 52°W in the analysis fields at 0000 UTC 1 September (Fig. 17b). The negative error plume then progressed west-northwestward in the 24-h AHW forecast from the 0000 UTC 1 September initialization (Fig. 17c).

7. Discussion

This paper reports on the development of a diagnostic approach that quantitatively examines the sources of error in forecast TC motion from numerical models. The motion error diagnostic equation was examined from a statistical perspective for the 2008–10 North Atlantic TC seasons, and in detailed case studies of TCs Earl and Fiona from the 2010 North Atlantic TC season. Twenty-four hour TC motion forecasts from the 2011 version of the Advanced Hurricane Weather Research and Forecasting Model (AHW; Skamarock et al. 2008; Davis

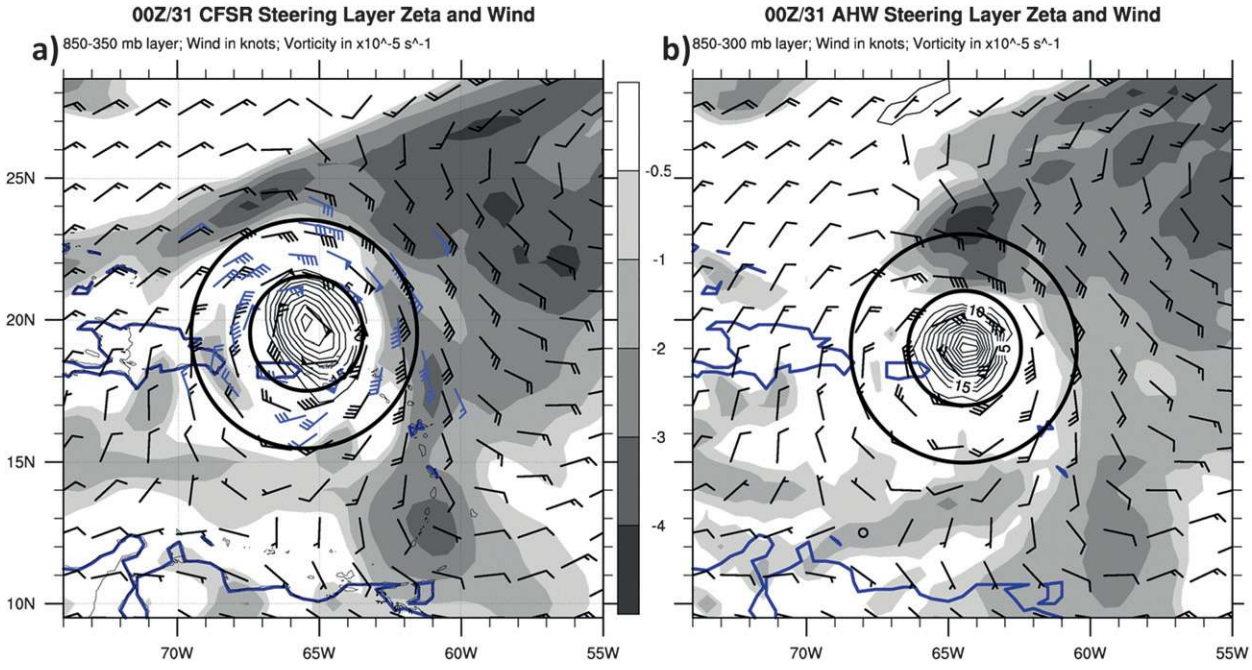

FIG. 14. (a) CFSR 0-h observed optimal steering layer (850–350 mb) and (b) AHW 24-h forecast optimal steering layer (850–300 mb) layer-average relative vorticity (contours with anticyclonic vorticity shaded in 10^{-5} s^{-1}) and layer-average wind (half barb = 2.5 m s^{-1}; full barb = 5.0 m s^{-1}; pennant = 25.0 m s^{-1}) verifying at 0000 UTC 31 Aug 2010. The 2° and 4° TC removal radii are labeled by the black circles. The blue wind barbs are observed 700-mb winds from time–space-corrected dropsondes taken during 1756–2322 UTC 30 Aug 2010 on a reconnaissance flight [data available online at http://www.aoml.noaa.gov/hrd/Storm_pages/earl2010/sonde.html].

et al. 2008a)—run retrospectively on the 2008–10 TC seasons—were the subject of this diagnostic analysis. The key findings from the paper are as follows.

We computed an optimal steering flow that allowed the TC removal radius and vertical depth to vary, which minimized the steering residual error with TC motion. The optimal steering layer shows an improvement over the DLM steering method, with a robust reduction in the scatter of the steering residual error distribution, highlighting that allowing two degrees of freedom on the steering flow calculation sharpens the agreement between steering flow and TC motion. The close match between the TC motion and the optimal steering flow allows us to meaningfully partition the difference in steering flow into errors in environment wind, vertical steering depth, and TC removal radius. Errors associated with beta effect are generally included in environment and radius errors; that they are generated by the TC circulation itself is not important for the present analysis.

For all 24-h AHW forecasts from the 2008–10 North Atlantic seasons, the storm motion error diagnostic equation showed that $\mathbf{v}_{\text{env}}$ errors are the most significant contributor to storm motion errors. Additionally, the storm motion vector error is frequently in the opposite direction of the 850–200-mb vertical wind shear. This result suggests that convection for vertically sheared TCs in AHW may be too symmetric, which limits downshear propagation of the TC. The structure and behavior of convection in TCs in AHW is the subject of future research. The case studies of TC Earl and Fiona showed that the large motion errors in the 24-h AHW forecasts—which led to large position errors at longer forecast times—were driven primarily by errors in the environment wind within the steering layer in agreement with the statistics from the 2008–10 North Atlantic seasons. The environment wind errors arose from persistent negative geopotential height errors in the subtropical ridge over the North Atlantic basin. The errors produced a westerly (northerly) wind perturbation in TC Earl's (Fiona's) environment contributing to the characteristic ''slow'' bias. This error might appear to be opposite of that reported in Torn and Davis (2012), who discussed errors associated with the treatment of shallow convection in AHW. However, the addition of the Tiedtke shallow convection scheme reduced the strength of easterlies in both studies, but in 2010, the abundance of storms in the central and eastern North Atlantic revealed the underestimate of easterlies in that region.

In addition to the persistent environment wind errors, at individual times errors associated with either the vertical steering depth or the TC removal radius contributed

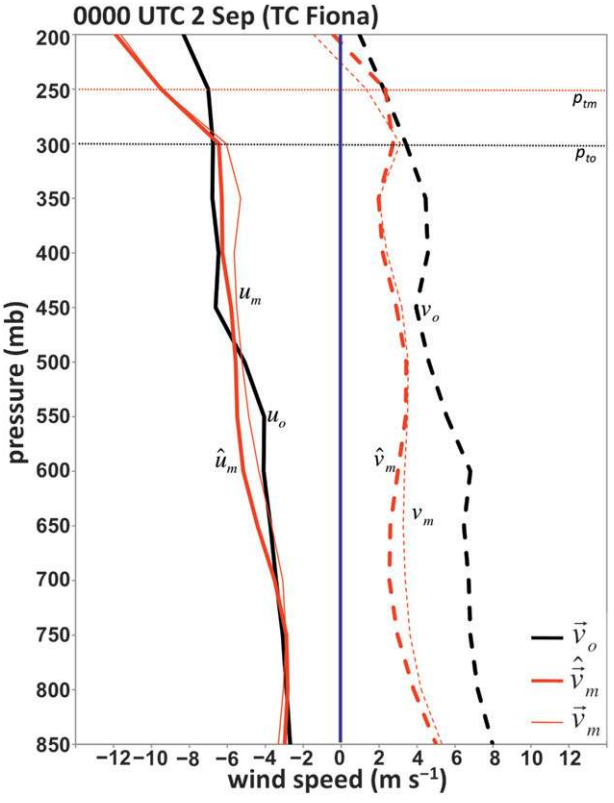

FIG. 15. As in Fig. 9, but for TC Fiona at 0000 UTC 2 Sep 2010.

to the 24-h AHW forecast TC motion errors. For example, errors associated with the TC removal radius were relatively large for TC Earl in the 24-h AHW forecast verifying at 0000 UTC 31 August. The TC removal radius error was related to differences in horizontal scale of the vortex and the presence of near-storm vorticity asymmetries. The vertical steering depth term was relatively large in the TC Earl AHW forecasts verifying at 0000 UTC 27 and 29 August. The key result here is that differences in the vertical depth of the AHW and observed vortex became more important in situations when a synoptic-scale feature in the upper troposphere (e.g., upper-level trough) induced flow over the TC center. Additionally, although the radius and steering depth terms were not significantly larger than the residual term on average when examining the long-term model biases over several seasons (e.g., Fig. 6), these terms can still dominate the residual at individual forecast times allowing for a valid physical interpretation of these terms.

In all, the storm motion error diagnostic equation highlights that AHW forecast storm motion errors—and by extension, position forecast errors—are consistent with previous studies that examined the global operational models in that motion errors are primarily related $\mathbf{v}_{\text{env}}$ errors in conjunction with structural and position errors of synoptic-scale features. We have developed and presented a new diagnostic approach that can be used to quantify these effects that contribute to forecast storm motion errors. The utility of the diagnostic equation is that it can be used for any numerical model output at a wide range of horizontal and vertical resolutions. The diagnostic equation points us where to look for the underlying causes of forecast errors, and allows quantification of the intersection between TC structure and position (i.e., track) errors. For example, in AHW the storm motion error diagnostic suggested that the systematic westerly $\mathbf{v}_{\text{env}}$ errors were associated with a subtropical ridge that is too weak. Preliminary work has pointed to reduced low-level heating in conjunction with a lack of aerosol treatment in the 2011 version of AHW as the primary contributor to reduced midlevel geopotential heights in the subtropics, and hence, a weaker subtropical ridge. Both TC Earl and Fiona occurred during a robust outbreak of dusty Saharan air of which AHW did not account for, and may explain in part the persistently weaker subtropical ridge in AHW.

In addition to evaluating TC motion forecasts in post event research mode as presented herein, the storm motion error diagnostic could be run in real-time operational mode. One potential methodology to consider would be to compute the storm error diagnostic on 24-h model forecasts compared to the GFS or European Centre for Medium-Range Weather Forecasts (ECMWF) analysis fields. This type of product would have a time lag of 1 day, but would give the forecasters clues as to what types of physical processes were contributing to motion errors in previous forecasts from a given model. Another methodology to consider would be to compare 24-h forecasts among different numerical weather prediction models. This type of product would alert forecasters to the physical processes that may be causing the motion forecasts from regional models to depart from the global models, for example. Alternatively, the motion error diagnostic equation could also be computed on ensemble forecasts from any operational center that compare the individual perturbation members to the control run and quantitatively show the processes in the ensemble that are contributing to ensemble spread in the track forecasts. That the motion error diagnostic can be run on any numerical model allows for flexibility when implementing the diagnostic in either research or operational mode.

Acknowledgments. This study benefited from discussions with Drs. Ryan Torn (University at Albany), John Molinari (University at Albany), Mike Fiorino (NOAA/ESRL-GSD), and Mark DeMaria (NOAA/

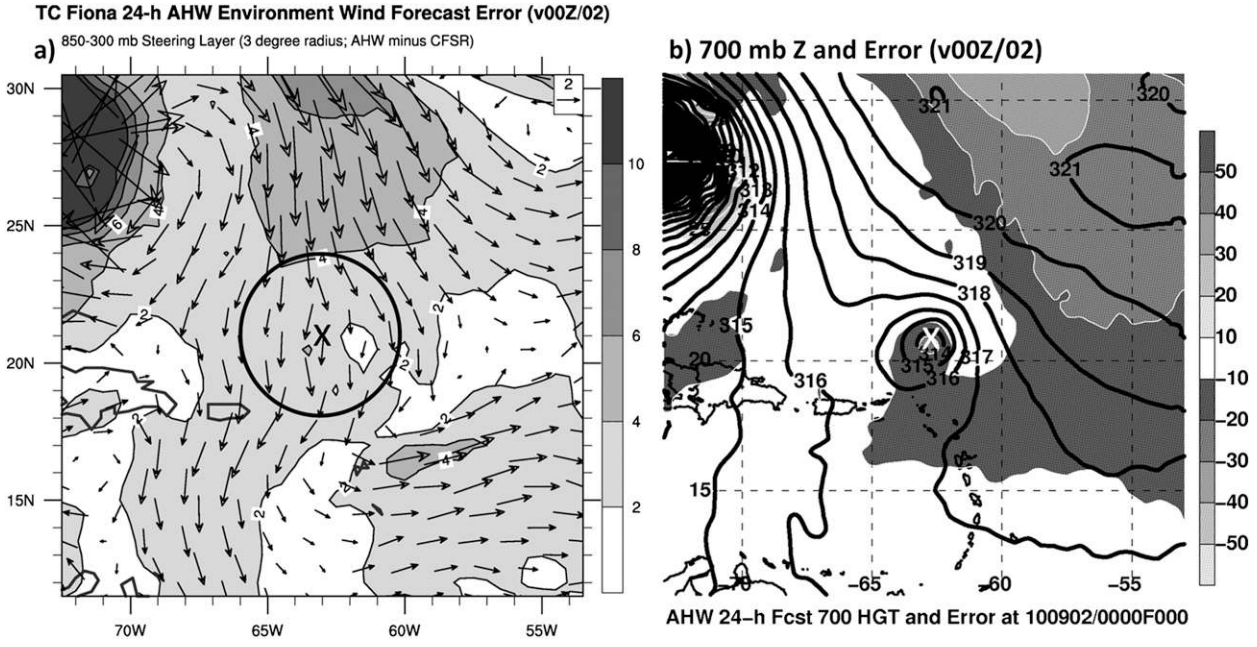

FIG. 16. AHW 24-h forecast (a) environment wind vector error (AHW − CFSR; arrows with magnitude shaded with contours according to the grayscale in m s^{-1}) vertically averaged in the observed optimal steering layer, and (b) 700-mb geopotential height (solid contours every 1 dam) and height error (AHW − CFSR; shaded according to the grayscale in m) verifying at 0000 UTC 2 Sep 2010. The grids are shifted so the forecast and observed TC are located at the same position marked 'X'. The radius of TC removal is marked by the range ring on the left panel.

NESDIS-RAMM). Sherrie Fredrick (NCAR) and Dave Ahijevych (NCAR) are thanked for providing technical support. The authors thank Dr. James Done (NCAR) for his valuable comments on the manuscript. Comments from three anonymous reviewers helped to improve the manuscript. This research was funded by the Hurricane Forecast Improvement Program (HFIP).

APPENDIX

Derivation of the TC Motion Error Diagnostic Equation

The aim of this appendix is to present the full derivation for the TC motion error diagnostic equation shown in (10). Recall from (9) that the model optimal steering layer flow, defined as the vertical pressure-weighted average of the area-average environment wind ($\mathbf{v}_m$), can be equated to the forecasted TC motion ($\mathbf{V}_m$) as

$$\mathbf{V}_m = \frac{1}{p_b - p_{t,m}} \int_{p_{t,m}}^{p_b} \mathbf{v}_m \, dp. \tag{A1}$$

To develop an environment wind error term in the motion error diagnostic equation, we need to include the model environment wind that is computed using the optimal radius for the observed TC $\hat{\mathbf{v}}_m$. We include this term on the right-hand side of (A1) to get

$$\mathbf{V}_m = \frac{1}{p_b - p_{t,m}} \int_{p_{t,m}}^{p_b} (\hat{\mathbf{v}}_m - \hat{\mathbf{v}}_m + \mathbf{v}_m) \, dp. \tag{A2}$$

We now separate the wind terms inside the bracket on the right-hand side of (A2) to get

$$\mathbf{V}_m = \frac{1}{p_b - p_{t,m}} \int_{p_{t,m}}^{p_b} \hat{\mathbf{v}}_m \, dp - \frac{1}{p_b - p_{t,m}} \int_{p_{t,m}}^{p_b} \hat{\mathbf{v}}_m \, dp + \frac{1}{p_b - p_{t,m}} \int_{p_{t,m}}^{p_b} \mathbf{v}_m \, dp. \tag{A3}$$

Now we split the integral in the first term in (A3) to include the observed steering depth p_o and then combine the second and third term in (A3) to produce the TC removal radius error term resulting in

$$\mathbf{V}_m = \frac{1}{p_b - p_{t,m}} \int_{p_{t,m}}^{p_{t,o}} \hat{\mathbf{v}}_m \, dp + \frac{1}{p_b - p_{t,m}} \int_{p_{t,o}}^{p_b} \hat{\mathbf{v}}_m \, dp + \frac{1}{p_b - p_{t,m}} \int_{p_{t,m}}^{p_b} -(\hat{\mathbf{v}}_m - \mathbf{v}_m) \, dp. \tag{A4}$$

We then algebraically manipulated the second term and rearranged the first two terms in (A4) to get

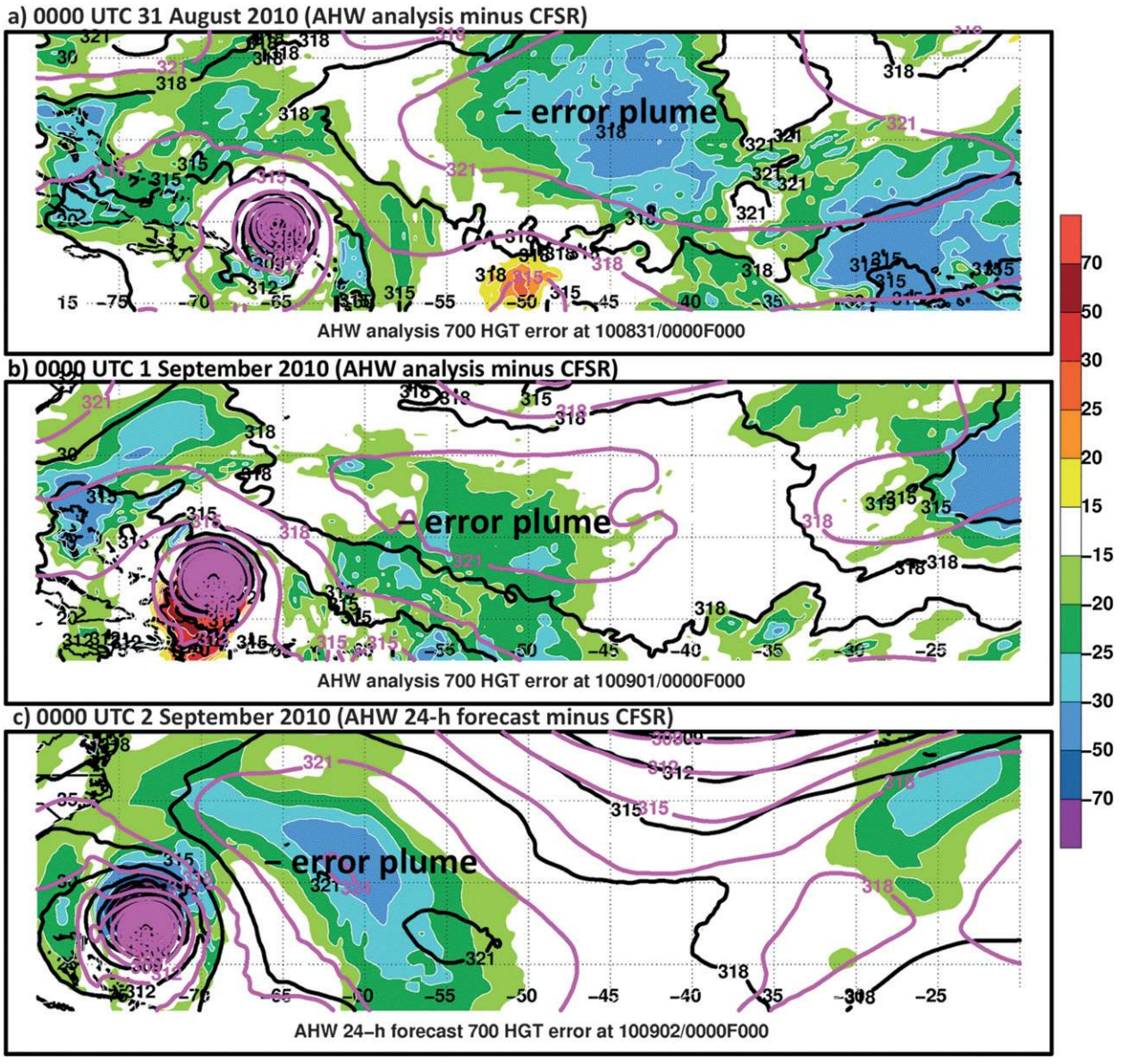

FIG. 17. The 700-mb geopotential height (solid contours every 3 dam; AHW in black; CFSR in magenta) and geopotential height analysis error (AHW − CFSR; shaded according to the color bar in m) verifying at 0000 UTC (a) 31 Aug and (b) 1 Sep. (c) As in (a),(b), but for AHW 24-h forecast error verifying at 0000 UTC 2 Sep. The negative height error ''plume'' is indicated on each panel.

$$\mathbf{V}_m = \frac{1}{p_b - p_{t,o}}\int_{p_{t,o}}^{p_b} \hat{\mathbf{v}}_m\, dp + \frac{p_{t,m} - p_{t,o}}{(p_b - p_{t,o})(p_b - p_{t,m})}\int_{p_{t,o}}^{p_b} \hat{\mathbf{v}}_m\, dp + \frac{1}{p_b - p_{t,m}}\int_{p_{t,m}}^{p_{t,o}} \hat{\mathbf{v}}_m\, dp + \frac{1}{p_b - p_{t,m}}\int_{p_{t,m}}^{p_b} -(\hat{\mathbf{v}}_m - \mathbf{v}_m)\, dp. \quad \text{(A5)}$$

The second and third terms in (A5) were combined and terms two–four in (A5) were rearranged resulting in

$$\mathbf{V}_m = \frac{1}{p_b - p_{t,o}}\int_{p_{t,o}}^{p_b} \hat{\mathbf{v}}_m\, dp + \frac{1}{p_b - p_{t,m}}\int_{p_{t,m}}^{p_b} -(\hat{\mathbf{v}}_m - \mathbf{v}_m)\, dp + \frac{1}{p_b - p_{t,m}}\left[\frac{p_{t,m} - p_{t,o}}{(p_b - p_{t,o})}\int_{p_{t,o}}^{p_b} \hat{\mathbf{v}}_m\, dp + \int_{p_{t,m}}^{p_{t,o}} \hat{\mathbf{v}}_m\, dp\right], \quad \text{(A6)}$$

which is the new definition for TC motion in the numerical model forecast. The first term in (A6) is the

model environment wind using the optimal radius and depth for the observed TC. The second term in (A6) is the flow resulting from differences in TC removal radius between the model and observed TC. The third term in (A6) is the flow resulting from differences in steering layer depth between the model and observed TC.

Recall from (8) that the observed optimal steering flow (computed from numerical model analysis fields such as the CFSR), can be equated to observed TC motion ($\mathbf{V}_o$) as

$$\mathbf{V}_o = \frac{1}{p_b - p_{t,o}} \int_{p_{t,o}}^{p_b} \mathbf{v}_o \, dp. \tag{A7}$$

Subtract (A7) from (A6) to get the storm motion error diagnostic equation [shown by (10) and described in detail in section 2c]:

$$\begin{aligned} \mathbf{V}_m - \mathbf{V}_o = & \frac{1}{p_b - p_{t,o}} \int_{p_{t,o}}^{p_b} (\hat{\mathbf{v}}_m - \mathbf{v}_o) \, dp \\ & + \frac{1}{p_b - p_{t,m}} \int_{p_{t,m}}^{p_b} -(\hat{\mathbf{v}}_m - \mathbf{v}_m) \, dp \\ & + \frac{1}{p_b - p_{t,m}} \left[\frac{p_{t,m} - p_{t,o}}{(p_b - p_{t,o})} \int_{p_{t,o}}^{p_b} \hat{\mathbf{v}}_m \, dp + \int_{p_{t,m}}^{p_{t,o}} \hat{\mathbf{v}}_m \, dp \right]. \end{aligned} \tag{A8}$$

REFERENCES

Aberson, S. D., 2010: 10 years of hurricane synoptic surveillance (1997–2006). *Mon. Wea. Rev.,* **138,** 1536–1549.

Bender, M. A., I. Ginis, and Y. Kurihara, 1993: Numerical simulation of tropical cyclone–ocean interaction with a high-resolution coupled model. *J. Geophys. Res.,* **98** (D12), 23 245–23 263.

Berg, R., 2010: Tropical cyclone report: Tropical Storm Fiona. Tech. Rep. AL082010, NOAA/National Hurricane Center, 13 pp. [Available online at http://www.nhc.noaa.gov/pdf/TCR-AL082010_Fiona.pdf.]

Brennan, M. J., and S. J. Majumdar, 2011: An examination of model track forecast errors for Hurricane Ike (2008) in the Gulf of Mexico. *Wea. Forecasting,* **26,** 848–867.

Cangialosi, J. P., 2011: Tropical Cyclone Report: Hurricane Earl. Tech. Rep. AL072010, NOAA/National Hurricane Center, 29 pp. [Available online at http://www.nhc.noaa.gov/pdf/TCR-AL072010_Earl.pdf.]

Carr, L. E., and R. L. Elsberry, 1990: Observational evidence for predictions of tropical cyclone propagation relative to environmental steering. *J. Atmos. Sci.,* **47,** 542–546.

——, and ——, 2000: Dynamical tropical cyclone track forecast errors. Part I: Tropical region error sources. *Wea. Forecasting,* **15,** 641–661.

Chan, J. C. L., and W. M. Gray, 1982: Tropical cyclone movement and surrounding flow relationships. *Mon. Wea. Rev.,* **110,** 1354–1374.

——, Y. Duan, and L. K. Shay, 2001: Tropical cyclone intensity change from a simple ocean–atmosphere coupled model. *J. Atmos. Sci.,* **58,** 154–172.

——, F. M. F. Ko, and Y. M. Lei, 2002: Relationship between potential vorticity tendency and tropical cyclone motion. *J. Atmos. Sci.,* **59,** 1317–1336.

Chou, M.-D., and M. J. Suarez, 1994: An efficient thermal infrared radiation parameterization for use in general circulation models. Tech. Rep., NASA Tech. Memo. 104606, 3, 85 pp.

Corbosiero, K. L., and J. Molinari, 2002: The effects of vertical wind shear on the distribution of convection in tropical cyclones. *Mon. Wea. Rev.,* **130,** 2110–2123.

Davis, C., and Coauthors, 2008a: Prediction of landfalling hurricanes with the Advanced Hurricane WRF model. *Mon. Wea. Rev.,* **136,** 1990–2005.

——, C. Snyder, and A. C. Didlake, 2008b: A vortex-based perspective of eastern Pacific tropical cyclone formation. *Mon. Wea. Rev.,* **136,** 2461–2477.

Dee, D. P., and Coauthors, 2011: The ERA-Interim reanalysis: Configuration and performance of the data assimilation system. *Quart. J. Roy. Meteor. Soc.,* **137,** 553–597.

Dong, K., and C. J. Neumann, 1986: The relationship between tropical cyclone motion and environmental geostrophic flows. *Mon. Wea. Rev.,* **114,** 115–122.

Ek, M. B., K. E. Mitchell, Y. Lin, E. Rogers, P. Grunmann, V. Koren, G. Gayno, and J. D. Tarpley, 2003: Implementation of Noah land surface model advances in the National Centers for Environmental Prediction operational mesoscale Eta model. *J. Geophys. Res.,* **108,** 8851, doi:10.1029/2002JD003296.

Fiorino, M., and R. L. Elsberry, 1989: Some aspects of vortex structure related to tropical cyclone motion. *J. Atmos. Sci.,* **46,** 975–990.

George, J. E., and W. M. Gray, 1976: Tropical cyclone motion and surrounding parameter relationships. *J. Appl. Meteor.,* **15,** 1252–1264.

Gray, W. M., 1994: Tropical cyclone propagation. Tech. Rep. ADA327290, Office of Naval Research, 38 pp. [Available online at www.dtic.mil/docs/citations/ADA327290.]

Hamill, T. M., J. S. Whitaker, D. T. Kleist, M. Fiorino, and S. G. Benjamin, 2011: Predictions of 2010's tropical cyclones using the GFS and ensemble-based data assimilation methods. *Mon. Wea. Rev.,* **139,** 3243–3247.

Holland, G. J., 1983: Tropical cyclone motion: Environmental interaction plus a beta effect. *J. Atmos. Sci.,* **40,** 328–342.

——, 1984: Tropical cyclone motion: A comparison of theory and observation. *J. Atmos. Sci.,* **41,** 68–75.

Hong, S.-Y., J. Dudhia, and S.-H. Chen, 2004: A revised approach to ice microphysical processes for the bulk parameterization of clouds and precipitation. *Mon. Wea. Rev.,* **132,** 103–120.

——, Y. Noh, and J. Dudhia, 2006: A new vertical diffusion package with an explicit treatment of entrainment processes. *Mon. Wea. Rev.,* **134,** 2318–2341.

Jarvinen, B. R., C. J. Neumann, and M. A. S. Davis, 1984: A tropical cyclone data tape for the North Atlantic basin, 1886–1983: Contents, limitations, and uses. NOAA Tech. Memo. NWS NHC 22, 24 pp. [Available online at http://www.nhc.noaa.gov/pdf/NWS-NHC-1988-22.pdf.]

Kehoe, R. M., M. A. Boothe, and R. L. Elsberry, 2007: Dynamical tropical cyclone 96- and 120-h track forecast errors in the western North Pacific. *Wea. Forecasting,* **22,** 520–538.

Komaromi, W. A., S. J. Majumdar, and E. D. Rappin, 2011: Diagnosing initial condition sensitivity of Typhoon Sinlaku (2008) and Hurricane Ike (2008). *Mon. Wea. Rev.,* **139,** 3224–3242.

McTaggart-Cowan, R., L. F. Bosart, J. R. Gyakum, and E. H. Atallah, 2006: Hurricane Juan (2003). Part II: Forecasting and numerical simulation. *Mon. Wea. Rev.,* **134,** 1748–1771.

Mitchell, C. L., 1924: West Indian hurricanes and other tropical cyclones of the North Atlantic Ocean. U.S. Weather Bureau, Washington, DC, Supplement 24, 47 pp.

Mlawer, E. J., S. J. Taubman, P. D. Brown, M. J. Iacono, and S. A. Clough, 1997: Radiative transfer for inhomogeneous atmosphere: RRTM, a validated correlated-k model for the long-wave. *J. Geophys. Res.,* **102** (D14), 16 663–16 682.

Neumann, C. J., 1979: On the use of deep-layer-mean geopotential height fields in statistical prediction of tropical cyclone motion. Preprints, *Sixth Conf. on Probability and Statistics in Atmospheric Sciences,* Banff, Alberta, Canada, Amer. Meteor. Soc., 32–38.

Rappaport, E. N., and Coauthors, 2009: Advances and challenges at the National Hurricane Center. *Wea. Forecasting,* **24,** 395–419.

Raymond, D. J., and H. Jiang, 1990: A theory for long-lived mesoscale convective systems. *J. Atmos. Sci.,* **47,** 3067–3077.

Saha, S., and Coauthors, 2010: The NCEP Climate Forecast System Reanalysis. *Bull. Amer. Meteor. Soc.,* **91,** 1015–1057.

Sanders, F., A. L. Adams, N. J. B. Gordon, and W. D. Jensen, 1980: Further development of a barotropic operational model for predicting paths of tropical storms. *Mon. Wea. Rev.,* **108,** 642–654.

Shapiro, L. J., and J. L. Franklin, 1995: Potential vorticity in Hurricane Gloria. *Mon. Wea. Rev.,* **123,** 1465–1475.

Skamarock, W. C., and Coauthors, 2008: A description of the Advanced Research WRF version 3. NCAR Tech. Note NCAR/TN-475+STR, 125 pp.

Torn, R. D., and C. A. Davis, 2012: The influence of shallow convection on tropical cyclone track forecasts. *Mon. Wea. Rev.,* **140,** 2188–2197.

Velden, C. S., and L. M. Leslie, 1991: The basic relationship between tropical cyclone intensity and the depth of the environmental steering layer in the Australian region. *Wea. Forecasting,* **6,** 244–253.

Wang, Y., and G. J. Holland, 1996: Tropical cyclone motion and evolution in vertical shear. *J. Atmos. Sci.,* **53,** 3313–3332.

Wilks, D. M., 1995: *Statistical Methods in the Atmospheric Sciences: An Introduction.* Academic Press, 467 pp.

Wu, C.-C., and K. A. Emanuel, 1993: Interaction of a baroclinic vortex with background shear: Application to hurricane movement. *J. Atmos. Sci.,* **50,** 62–76.

Zhang, C., Y. Wang, and K. Hamilton, 2011: Improved representation of boundary layer clouds over the southeast Pacific in ARW-WRF using a modified Tiedtke cumulus parameterization scheme. *Mon. Wea. Rev.,* **139,** 3489–3513.